agronomy

Article

Agricultural Waste for Remediation of Neonicotinoid Pollution: Mechanisms and Environmental Effects of Multi-Site Adsorption of Dinotefuran on Rice Husk Biochar

Longfei Liu [1,2,*], Xinyu Jiang [1], Tianyu Lu [3] and Jinzhao Ma [4]

[1] College of Environmental Science and Engineering, Yangzhou University, Yangzhou 225127, China; mz120241367@stu.yzu.edu.cn
[2] Key Laboratory of Arable Land Quality Monitoring and Evaluation, Ministry of Agriculture and Rural Affairs, Yangzhou University, Yangzhou 225127, China
[3] Co-Innovation Center for the Sustainable Forestry in Southern China, College of Ecology and the Environment, Nanjing Forestry University, Nanjing 210037, China; lutianyu@njfu.edu.cn
[4] Shandong Key Laboratory of Eco-Environmental Science for the Yellow River Delta, Shandong University of Aeronautics, Binzhou 256603, China; mjz167448612@163.com
* Correspondence: liulongfei@yzu.edu.cn

Abstract

The increasing contamination of neonicotinoid pesticides in the environment has become a growing concern, and biochar is considered a promising strategy for removing these pollutants. This study converted waste rice husks into biochar (RHB) via pyrolysis at 400–600 °C under anaerobic conditions, using dinotefuran (DIN) as a representative neonicotinoid. The physicochemical properties of RHB and its adsorption mechanisms for DIN were systematically investigated. Results showed that higher pyrolysis temperatures increased the specific surface area, microporosity, and aromaticity of biochar, while altering the distribution of surface functional groups. RHB prepared at 600 °C (RHB600) exhibited the highest adsorption capacity. The adsorption process followed the Sips isotherm and pseudo-second-order kinetic models, indicating a spontaneous and endothermic process involving heterogeneous physic–chemical adsorption. The primary mechanisms included pore filling, π–π interactions, and hydrogen bonding. The sequence of functional group response during DIN adsorption was C–O > C=C > C=O > –OH. Environmental factors such as solution pH and humic acid concentration significantly influenced adsorption, while phosphate ions caused strong competitive inhibition. An artificial neural network model accurately predicted adsorption under multiple interacting factors, and RHB600 demonstrated good regeneration after ethanol elution. This study confirms that RHB is an effective and practical adsorbent, providing a technical reference for agricultural waste valorization and pesticide-polluted water remediation.

Keywords: rice husk biochar; new nicotine pesticides; adsorption mechanism; environmental applications

Academic Editor: Claudio Ciavatta

Received: 5 November 2025
Revised: 21 November 2025
Accepted: 26 November 2025
Published: 28 November 2025

Citation: Liu, L.; Jiang, X.; Lu, T.; Ma, J. Agricultural Waste for Remediation of Neonicotinoid Pollution: Mechanisms and Environmental Effects of Multi-Site Adsorption of Dinotefuran on Rice Husk Biochar. *Agronomy* **2025**, *15*, 2746. https://doi.org/10.3390/agronomy15122746

1. Introduction

Neonicotinoid insecticides (NEOs) are widely applied in agricultural activities worldwide due to their high broad-spectrum insecticidal activity [1]. It is noteworthy that only a small fraction (typically 2–20%) of applied NEOs is absorbed by crops, while the majority are released into the environment [2]. However, the environmental persistence and high water solubility of NEOs enable them to migrate into soils, surface waters, and even drinking water sources, posing serious risks to human health and ecosystems [2,3]. Recent studies have further corroborated the pervasive occurrence and associated risks of NEOs in diverse aquatic environments. For instance, an investigation of the Huaihe River Basin, a typical agricultural area, revealed that the total concentration of NEOs reached a maximum of 191.2 ng/L, with thiamethoxam being the dominant compound [4]. Research in water bodies connected to the South-to-North Water Diversion Project's Eastern Route found that the average total NEO concentration in Lake Hongze exceeded 200 ng/L across spring, summer, and winter [5]. Furthermore, NEOs have been frequently detected in the effluents of wastewater treatment plants across multiple Chinese cities [6]. A report showed an average NEO concentration of 130 ng/L in surface waters, with peak levels reaching 630 ng/L [7]. In agricultural areas, groundwater NEO concentrations can even reach 10,000 ng/L [8]. In some rivers in eastern China, NEO concentrations have exceeded acute (362 ng/L) and chronic (58 ng/L) ecological risk thresholds [9]. As a nitro-substituted compound, dinotefuran (DIN) exhibits higher toxicity and greater water solubility [2]. Therefore, these latest findings underscore the continued urgency of developing efficient and cost-effective technologies for removing NEOs from water.

Currently, various methods are employed to treat DIN-contaminated water, primarily including biodegradation, advanced oxidation processes, electrochemical methods, and adsorption [10–12]. Biodegradation involves high cultivation costs, and microorganisms are sensitive to environmental conditions (e.g., pH, temperature, coexisting substrates) with often incomplete degradation, making large-scale engineering applications challenging [1]. Advanced oxidation processes tend to generate a series of unknown intermediate products, which frequently exhibit higher toxicity than the parent compound [13]. Electrochemical methods require expensive electrode materials that are prone to passivation and deactivation, limiting their economic feasibility for large-scale applications [14]. In contrast, adsorption stands out due to its low cost, simple operation, high efficiency, and reusability of adsorbents, making it an ideal approach for pollutant removal [13,15,16]. Common adsorbents include minerals, polymeric materials, metal–organic frameworks, and biochar [13,17–19]. Among these, biochar has attracted significant research attention in recent years due to its excellent specific surface area (SSA), abundant functional groups, and proven effectiveness in removing both organic and inorganic contaminants [20].

Biochar is a solid material produced through the pyrolysis of biomass under oxygen-limited conditions. Its well-developed porosity, large SSA, and abundant oxygen-containing functional groups make it a promising material for treating organic pollution [20,21]. Converting rice husks into biochar via high-temperature pyrolysis represents a viable strategy to address their underutilization [22]. Rice husk–derived biochar shows broad potential for removing various pollutants from aquatic environments. For instance, Apolloni et al. reported that rice husk biochar could remove over 93% of atrazine and terbuthylazine via π–π interactions [23]. It has also been demonstrated to adsorb heavy metals and dyes through mechanisms such as surface complexation, ion exchange, electrostatic attraction, and hydrogen bonding [24,25]. Therefore, biochar produced from rice husks can serve as an effective adsorbent for the removal of organic pollutants from the environment.

Despite the growing body of research on biochar for water remediation, a systematic investigation into the adsorption of DIN by rice husk biochar (RHB) remains scarce. Specifically, the evolution of the dominant adsorption mechanism with biochar pyrolysis temperature, and a quantitative understanding of the energy heterogeneity of adsorption sites for DIN, are critically underexplored [13]. Furthermore, accurately predicting adsorption efficiency in realistic environments with multiple fluctuating factors (e.g., pH, organic matter) requires models that go beyond conventional single-factor analysis [26,27].

To address these knowledge gaps, this study not only evaluates the performance of RHB but also employs a suite of advanced diagnostic and modeling techniques to deliver deeper mechanistic and practical insights. Specifically, site energy distribution (SED) analysis was applied to quantitatively characterize the energy heterogeneity of RHB surfaces, moving beyond the assumption of homogeneous sites [28]. Response surface methodology (RSM) and artificial neural network (ANN) were utilized to decipher the complex, non-linear interactions of environmental factors and to provide a robust predictive tool for real-world application scenarios, a significant advancement over traditional one-variable-at-a-time approaches [29].

In this study, a simple and sustainable approach was adopted, converting waste rice husk biomass into biochar at different pyrolysis temperatures. This work investigated the effectiveness of rice husk biochar (RHB) in removing DIN from aqueous environments. The research specifically focused on: (1) examining the adsorption behavior and binding processes of DIN onto RHB through kinetic and isotherm studies; (2) determining the energy distribution during adsorption using site energy distribution analysis; (3) evaluating the interactive effects of various environmental factors on DIN adsorption by RHB employing Response Surface Methodology and Artificial Neural Network models; and (4) elucidating the underlying adsorption mechanisms. Through this integrated approach, this study aims to provide a comprehensive understanding of the adsorption process and to firmly establish the valorization of rice husk waste as a sustainable strategy for mitigating nitrogen-based pesticide pollution, contributing to the circular economy in agriculture.

2. Materials and Methods

2.1. Materials

Rice husks were obtained from a local market in Yangzhou, Jiangsu Province, China. Dinotefuran (DIN), humic acid (HA), NaCl, $CaCl_2$, KCl, $FeCl_3$ and anhydrous ethanol were purchased from Shanghai Macklin Biochemical Technology Co., Ltd. (Shanghai, China) and used without further purification.

2.2. Preparation of RHB

RHB was produced via anaerobic pyrolysis. Briefly, the rice husks were washed with deionized water to remove impurities, oven-dried at 60 °C, and then crushed using a mechanical grinder. The crushed rice husks were subsequently sieved to obtain a uniform particle size fraction between 10 and 20 mesh (0.85–2.00 mm), ensuring consistent pyrolysis conditions and adsorption characteristics. These sieved particles were placed in a tubular furnace under a continuous N_2 atmosphere (flow rate: 100 mL/min). The pyrolysis was conducted with a heating rate of 5 °C/min. Once the temperature reached 400 °C, it was maintained for 2 h. The resulting material was allowed to cool naturally to room temperature. The primary biochar was then rinsed with deionized water to remove water-soluble organic carbon and dried at 60 °C to obtain the final product, designated as RHB400. The dried RHB400 was further sieved through a 40-mesh screen (<0.425 mm) to obtain a uniform fraction for adsorption experiments. Using the same procedure, biochars produced at 500 °C and 600 °C were labeled RHB500 and RHB600, respectively.

2.3. Batch Adsorption Experiments

2.3.1. Adsorption Kinetics

Batch experiments were conducted to study the adsorption of DIN onto RHB. To investigate the adsorption kinetics, 0.02 g of RHB was added to a sealed vial containing 20 mL of a 40 mg/L DIN solution. The initial pH of the solution was adjusted to 6.5 ± 0.3 using 0.1 M HCl or NaOH, and no buffer was used. The vials were shaken at 150 rpm in a constant-temperature shaker at 25 °C. Samples were taken at predetermined time intervals (0, 5, 10, 20, 30, 60, 120, 180, 240, 300, 360, 720 and 1440 min), immediately filtered through 0.45 µm nylon membranes, and the pH of the filtrate was measured before quantifying the DIN concentration in the supernatant was quantified using High-Performance Liquid Chromatography (HPLC). The final pH of the mixture at equilibrium was measured to be in the range of 9.25–10.23 across all RHB types, consistent with their alkaline nature (Table 1). All treatments were performed in triplicate.

Table 1. Physical-chemical properties of RHB.

Adsorbent	pH	SSA (m^2/g)	PV (cm^3/g)	Pore Size (nm)	Ash (%)	Element Content (%)				Atomic Ratio		
						C	H	N	O	H/C	O/C	(O + N)/C
RHB400	9.81	22.04	0.0663	15.31	35.42	52.38	3.37	0.68	8.15	0.0643	0.1556	0.1686
RHB500	10.03	28.37	0.1082	7.87	40.61	44.67	2.41	0.52	11.79	0.0540	0.2639	0.2756
RHB600	10.29	38.41	0.1206	4.08	42.39	41.02	2.19	0.44	13.96	0.0534	0.3403	0.3510

2.3.2. Adsorption Isotherms

Adsorption isotherms were used to evaluate the adsorption capacity and binding behavior. The equilibrium contact time for isotherm experiments was determined based on preliminary kinetic studies and pre-experiments, which confirmed that adsorption equilibrium between DIN and RHB was achieved within 4 h. However, to ensure complete equilibrium under all experimental conditions and to account for potential variations at higher initial DIN concentrations, a conservative contact time of 24 h was selected for all isotherm experiments. A mass of 0.02 g of RHB was introduced into a series of 20 mL DIN solutions with initial concentrations ranging from 2 to 40 mg/L. The initial pH of all solutions was adjusted to 6.5 ± 0.3. The vials were then shaken at 150 rpm at 25 °C for 24 h to reach equilibrium. After filtration through 0.45 µm membranes, the equilibrium concentration of DIN was measured by HPLC. Each experiment was carried out in triplicate.

2.3.3. Adsorption Thermodynamics

The thermodynamic parameters of the adsorption process were determined by conducting isotherm experiments at three different temperatures: 288.15 K, 298.15 K, and 308.15 K. The specific calculation formulas for thermodynamic parameters (ΔH°, ΔS°, ΔG°) are placed in the Supplementary Materials (Part I). The procedure was identical to that described in Section 2.3.2. All tests were performed in triplicate.

2.3.4. Influence of Environmental Factors

The effects of various environmental factors on DIN adsorption were investigated, including biochar dosage (0.01–0.05 g), solution pH (3–11), ionic strength (0–20 mM), cation type (Na^+, K^+, Ca^{2+}, Fe^{3+}), anion type (NO^{3-}, PO_4^{3-}, Cl^-, SO_4^{2-}), and HA concentration (0–20 mg/L). The concentration of this experiment was set based on the concentration of various substances in the natural water environment [30,31]. Briefly, the ionic strength was adjusted using NaCl as background electrolyte. For cation/anion competition experiments, chloride salts (NaCl, KCl, $CaCl_2$, $FeCl_3$) were used for cations, while sodium salts ($NaNO_3$, NaCl, Na_2SO_4, Na_3PO_4) were used for anions, all at a fixed concentration of 10 mM. HA stock solution (1000 mg/L) was prepared by dissolving commercial HA in 0.01 M NaOH, adjusting pH to 7.0 with 0.1 M HCl, and filtering through a 0.45 µm membrane to remove undissolved residues, according to the International Humic Substances Society (IHSS) standard protocol. Working solutions of desired HA concentrations were freshly prepared by diluting the stock solution with background electrolyte (1 mM NaCl) immediately before experiments. A control variable approach was used for single-factor experiments, where only one parameter was changed while others were kept constant. The initial DIN concentration was fixed at 20 mg/L, and the solution pH was adjusted to 6.5 ± 0.3 with 0.1 M HCl or NaOH unless otherwise specified for pH-dependent experiments. All experiments were conducted in triplicate.

Furthermore, a Central Composite Design (CCD) was employed to study the interactive effects of three key factors (pH, ionic strength (IS), and HA concentration, each at five levels, see Table S1). This design generated 60 experimental runs. Analysis of Variance (ANOVA) was used to analyze the individual and interactive effects of these variables on DIN removal. The results were further modeled and analyzed using Response Surface Methodology (RSM) and an Artificial Neural Network (ANN). The development of the ANN model followed a standardized procedure to ensure robustness and reproducibility. A feedforward neural network with a single hidden layer and an output layer was constructed. The optimal number of neurons in the hidden layer was determined to be 5 through an iterative trial-and-error process aimed at minimizing the mean squared error. The input layer consisted of three neurons corresponding to the three independent variables (pH, IS, HA concentration), and the output layer had one neuron representing the predicted DIN removal efficiency (Figure S1). The hyperbolic tangent sigmoid (tansig) and linear (purelin) transfer functions were used in the hidden and output layers, respectively. The Levenberg–Marquardt algorithm was employed for network training. The full dataset from the CCD data points) was randomly divided into three subsets: 70% for training, 15% for validation, and 15% for testing. Both RSM (Equation (1)) and ANN demonstrated accurate simulation and prediction of the response under varying conditions. The RSM analysis was performed using Design-Expert 13 (Stat-Ease, Inc., Minneapolis, MN, USA), while the ANN model was developed in MATLAB R2021b (MathWorks, Inc., Natick, MA, USA).

$$y = b_0 + \sum_{i=1}^{N} b_i x_i + \sum_{i=1}^{N} b_{ii} x_i^2 + \sum_{i=1,j=1}^{N} b_{ij} x_i x_j + \varepsilon \tag{1}$$

where y is the predicted DIN removal efficiency, x_i and x_j are the independent variables, b_0 is the constant coefficient, b_i is the linear coefficient, b_{ii} is the quadratic coefficient, b_{ij} is the interaction coefficient, and ε is the error term.

2.4. Reusability Performance

The reusability of RHB600 was evaluated through five consecutive adsorption–desorption cycles. After the adsorption phase, the spent RHB600 was separated and treated with 0.2 M HCl, 0.2 M NaOH, or ethanol as desorbing agents. The desorption procedure mirrored the adsorption experiment, employing the same contact time (24 h), shaking speed (150 rpm), temperature (25 °C), and solid–liquid ratio (1 g/L, i.e., 0.02 g biochar in 20 mL desorbent), with the only change being the replacement of the background solution with the respective desorbent. The concentration of DIN in the desorption filtrate was measured to determine the desorption efficiency.

2.5. Characterization

The SSA and pore size distribution of the biochars were analyzed using a surface area and porosity analyzer (ASAP 2460, Micromeritics, Norcross, GA, USA). Prior to analysis, samples were degassed at 150 °C under vacuum for 12 h to remove adsorbed moisture and contaminants. Nitrogen adsorption–desorption isotherms were measured at 77 K, and SSA was calculated using the Brunauer–Emmett–Teller. Pore size distribution was determined using the density functional theory model. The micro-morphology was examined by Scanning Electron Microscopy (SEM, JEOL JSM-7900F, Hitachi, Tokyo, Japan).

To enhance conductivity, the biochar samples were sputter-coated with a thin layer of gold before imaging. Surface functional groups were identified using Fourier Transform Infrared Spectroscopy (FTIR, Cary 610/670, Agilent, Santa Clara, CA, USA). The FTIR spectra were recorded in the range of 4000–400 cm^{-1} with a resolution of 4 cm^{-1}, accumulating 32 scans per spectrum. Background correction was performed using a clean KBr pellet, and all sample spectra were baseline-corrected. The surface chemical composition before and after DIN adsorption was analyzed by X-ray Photoelectron Spectroscopy (XPS, ESCALAB 250Xi, Thermo Fisher Scientific, Waltham, MA, USA). The XPS analysis was conducted using a monochromatic Al Kα X-ray source (1486.6 eV). Survey and high-resolution spectra were collected with pass energies of 150 eV and 50 eV, respectively. All binding energies were calibrated by referencing the C 1s peak to 284.8 eV. The data were processed using Thermo Avantage (Thermo Fisher Scientific, Waltham, MA, USA), including background subtraction using a Shirley-type background and peak fitting with Gaussian-Lorentzian line shapes. The content of soluble metal elements in RHB was determined by Inductively Coupled Plasma Optical Emission Spectrometry (ICP-OES, Agilent 725-ES). The zeta potential was measured with a Zetasizer Nano ZS (Zetasizer Nano ZS, Malvern Panalytical, Great Malvern, UK). The elemental composition (C, H, N, O) was analyzed using an elemental analyzer (FlashSmart, Thermo Fisher Scientific, Waltham, MA, USA).

2.6. Density Functional Theory (DFT) Calculation

In the present investigation, computational models representing the aromatized carbon structure and key functional groups of high-temperature biochar were constructed using GaussView 6.0 software. All quantum chemical calculations were performed using the Gaussian 16 W software package. The geometry of all structures was fully optimized without any constraints using the B3LYP hybrid functional [32]. To accurately account for the dispersion interactions that are critical in π-system interactions, the Grimme's D3 empirical correction with Becke-Johnson damping (GD3BJ) was incorporated [33]. The 6–31G(d,p) Pople-style basis set was employed for all atoms, providing a balanced level of accuracy and computational cost for systems of this size.

The optimization calculations were considered converged when the following default thresholds in Gaussian 16 were met: the maximum force was less than 4.5×10^{-4} Hartree/Bohr, the root mean square (RMS) force was below 3.0×10^{-4} Hartree/Bohr, the maximum displacement was smaller than 1.8×10^{-3} Bohr, and the RMS displacement was below 1.2×10^{-3} Bohr. The self-consistent field (SCF) calculations were converged to a tolerance of 10^{-8} a.u. using the ultrafine integration grid (99, 590 points) to ensure high accuracy in numerical integration.

Following geometry optimization, frequency analyses were conducted at the same level of theory to confirm that the optimized structures were true local minima on the potential energy surface (no imaginary frequencies). Subsequently, single-point energy calculations were performed on the optimized geometries to compute the electrostatic potential (ESP). The EP maps were generated and visualized using the Multiwfn 3.8 package based on the calculated electron densities, allowing for a visual and quantitative analysis of the charge distribution and the identification of potential active sites for DIN interaction.

2.7. Data Processing

The kinetic data were fitted using the pseudo-first-order, pseudo-second-order, and intra-particle diffusion models. The equilibrium isotherm data were analyzed with the Langmuir, Freundlich, and Sips models. Detailed explanations of these models and their parameters are provided in the Supplementary Materials (Part I).

3. Results and Discussion

3.1. Characterization of RHB

As the pyrolysis temperature increased from 400 °C to 600 °C, the pH of RHB rose from 9.81 to 10.29, and the ash content increased from 35.42% to 42.39% (Table 1). The pore structure of RHB was simultaneously improved. The SSA increased from 22.04 m^2/g to 38.41 m^2/g, and the PV increased from 0.0663 cm^3/g to 0.1206 cm^3/g, while the average pore diameter decreased from 15.31 nm to 4.08 nm. Elemental composition analysis showed a decrease in the H/C ratio from 0.064 to 0.053, while the O/C and (O + N)/C ratios increased from 0.156 and 0.169 to 0.340 and 0.351, respectively.

These changes reflect the concurrent cracking of volatile components and condensation of the carbon skeleton during high-temperature pyrolysis. The increased aromaticity (lower H/C) and the formation of new pores led to more developed micro-/mesopores, resulting in higher SSA and pore volume (PV) (Figure S2) [34]. Simultaneously, oxides/carbonates such as SiO_2, K, Ca, and Mg, inherent to rice husks, became relatively enriched, increasing ash content and alkalinity [35]. The characterization results indicate that RHB600 relies more on pore-filling and hydrophobic effects for DIN adsorption, whereas the polar functional groups on RHB400 favor adsorption via hydrogen bonding and Lewis acid-base interactions [36].

The FTIR spectra (Figure S3) showed characteristic peaks that were assigned to key functional groups. The band at 790–820 cm^{-1} is predominantly attributed to the symmetric stretching vibration of Si–O–Si bonds [24,37], which is a characteristic feature of rice husk biochar due to its high silica content. While this region can potentially overlap with aromatic C–H out-of-plane bending, the assignment to Si–O–Si is strongly supported by the concurrent presence of the intense, broad band at 1000–1160 cm^{-1}, which corresponds to the asymmetric stretching of Si–O–Si [38]. The band at 1200–1270 cm^{-1} was assigned to C–O stretching in phenolic hydroxyl or ether groups. The spectral features in the 1510 cm^{-1} and 1600–1645 cm^{-1} regions are primarily attributed to the aromatic skeleton and C=C stretching vibrations, consistent with the developing aromaticity of the biochar as indicated by the decreasing H/C ratio [39]. It is noteworthy that these bands, particularly the one at ~1600 cm^{-1}, can also encompass overlapping contributions from stretching modes of conjugated carbonyl (C=O) groups or C=C in polycyclic aromatic structures [40]. Peaks in the 1720–1800 cm^{-1} range corresponded to C=O stretching in carbonyl and carboxyl groups [41]. Peaks at 2970–3000 cm^{-1} indicated the presence of aliphatic $–CH_2$ groups. RHB400 exhibited the most intense polar bands, suggesting that low-temperature pyrolysis preserved more carbonyl and ether groups, providing hydrogen bond donors/acceptors for DIN adsorption [36]. As the pyrolysis temperature increased, these polar sites were gradually removed or rearranged, while the aromatic skeleton and pore structure became more developed. Consequently, the aromatic C=C in RHB600 can engage in π–π interactions with the aromatic furan ring present in the DIN molecule [26,42]. The polar moieties of DIN (e.g., carbonyl and nitro groups) are primarily involved in hydrogen bonding, as discussed elsewhere.

Two-dimensional correlation spectroscopy (2D-COS) FTIR was used to further analyze the changes in functional groups with pyrolysis temperature (Figure 1). The synchronous spectrum (Figure 1a) showed positive cross-peaks in regions such as C=O—C-O (1250 × 1720 cm^{-1}), aromatic C=C—C–O (1250 × 1600 cm^{-1}), and O–H—Si–O–Si (3400 × 1100 cm^{-1}), indicating these groups changed in the same direction [43]. The asynchronous spectrum (Figure 1b), interpreted with Noda's rule, revealed the sequence of functional group changes: aromatic C=C > C=O > C–O. The O–H response preceded Si–O–Si, which in turn preceded Si–OH (~950 cm^{-1}) [43]. This sequential transformation aligns with the established thermal degradation kinetics of lignocellulosic biomass and biomineral frameworks. The initial reorganization of aromatic structures and oxygen-containing functional groups (below 500 °C) corresponds to the devolatilization and carbonization stages, where organic components decompose before significant inorganic transformations occur [44,45]. The subsequent changes in silicate structures (above 500 °C) reflect the temperature-dependent condensation kinetics of silica networks, where Si–O–Si bond formation and rearrangement proceed more slowly than organic matrix decomposition [44]. This delayed mineral framework reconstruction is characteristic of silica-rich biomass like rice husk, where the biogenic silica structure requires higher activation energy and longer residence time for structural reorganization compared to organic component degradation [46].

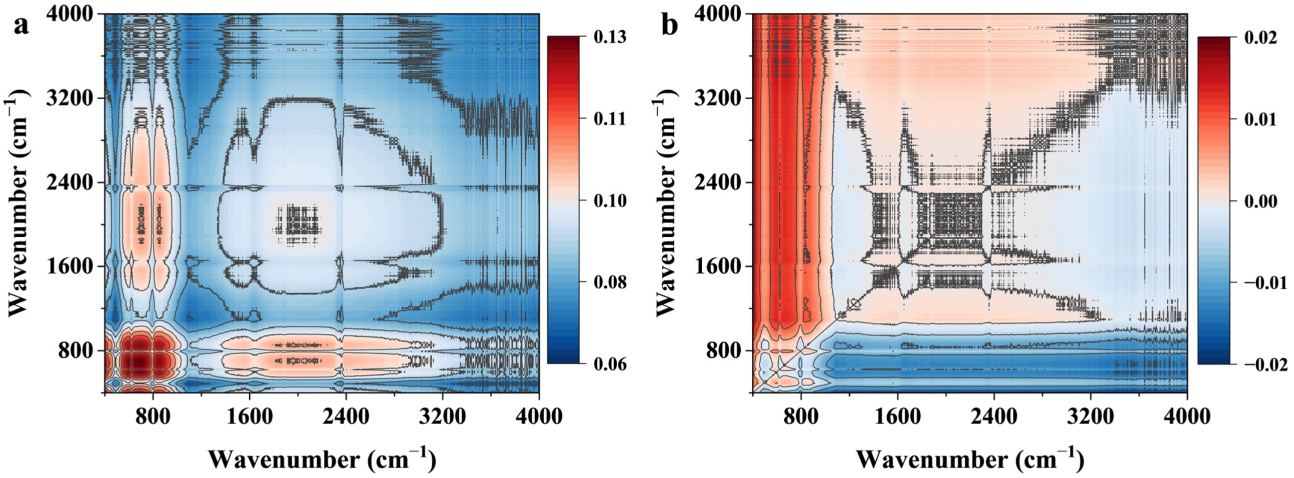

Figure 1. 2D-FTIR-COS (**a**) synchronous spectra and (**b**) asynchronous spectra of RHB.

These 2D-COS results indicate that with increasing pyrolysis temperature, the organic polar groups and aromatic framework of RHB undergo rapid reorganization and partial removal below 500 °C, while the mineral framework and surface silanols follow a slower, diffusion-limited reconstruction process above 500 °C [44,47–49]. This thermal evolution pattern suggests RHB400 primarily adsorbs DIN via polar sites and hydrogen bonding, while RHB600 tends to rely more on pore-filling, hydrophobic, and π–π interactions [27].

3.2. Adsorption Kinetics

The dynamic adsorption trends of DIN onto RHB400, RHB500, and RHB600 are shown in Figure 2a. All three RHBs exhibited a similar pattern: a rapid adsorption phase within 0–30 min, where over 80% of the total adsorption capacity was achieved, followed by a gradual slowdown between 30 and 120 min, eventually reaching equilibrium after 120 min. This is primarily because abundant vacant adsorption sites were available on the RHB surface initially, facilitating fast DIN attachment. As these sites became occupied over time, the availability decreased, leading to a reduced adsorption rate until equilibrium was established [26].

Different models provide insights into the dynamic adsorption characteristics. The pseudo-second-order model fitted the adsorption data better than the pseudo-first-order model (Table S2), suggesting the process involves both physisorption and chemisorption, with chemisorption being dominant. RHB600 exhibited a higher initial adsorption rate (higher v_0) compared to RHB400 and RHB500 [26]. The calculated initial adsorption rate (v_0) for RHB600 (2.01 mg g^{-1} min^{-1}) was substantially higher than values reported for dinotefuran adsorption on corn cob biochar (1.36 mg g^{-1} min^{-1}) [50], highlighting the superior kinetic performance of RHB600. The higher SSA, PV, developed microporosity, and exposed mineral-hydroxyl network of RHB600 provide more adsorption sites and stronger pore-filling capacity, leading to its superior initial rate and equilibrium capacity [26,27]. RHB400, with more polar functional groups but limited pore structure, relies on external surface sites and hydrogen bonding, which restricts its overall adsorption rate and capacity [20]. This trade-off between surface functionality and porous structure in governing adsorption kinetics has also been noted in studies on engineered biochars, but our results provide a clear quantitative illustration of this effect across a pyrolysis temperature gradient [26].

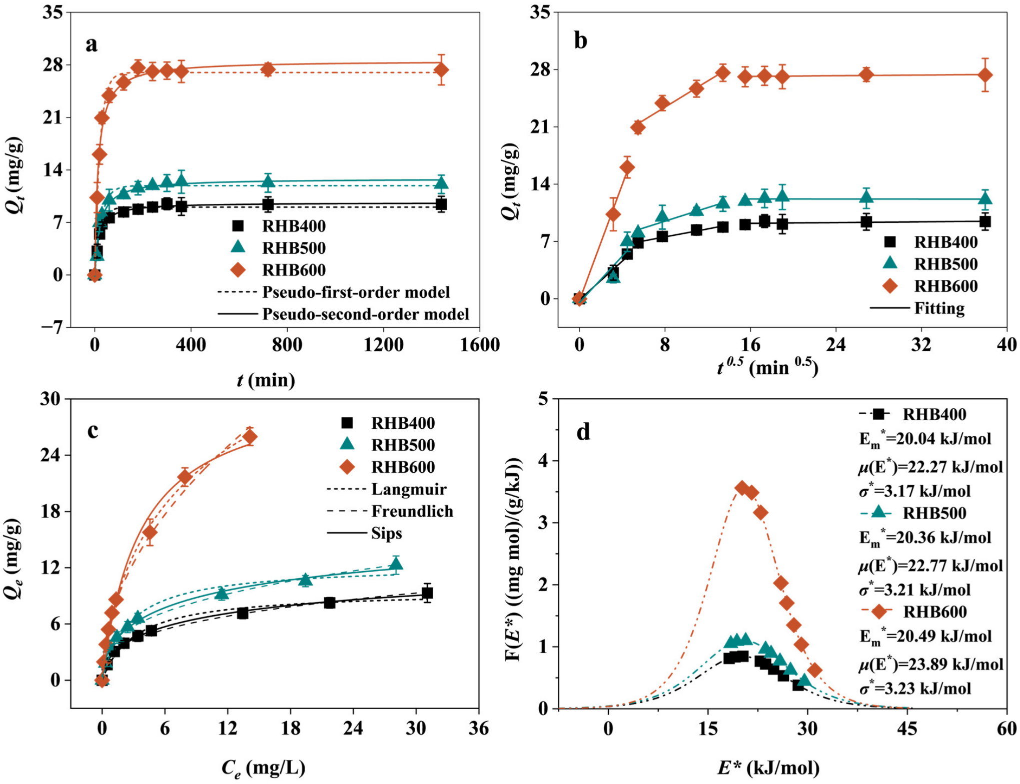

Figure 2. Adsorption kinetics data of DIN on RHB were fitted by (**a**) pseudo-first-order model and pseudo-second-order model, (**b**) intra-particle diffusion model. (**c**) Adsorption isotherm data were fitted by Langmuir, Freundlich and Sips model. (**d**) Site energy distribution of RHB.

The intra-particle diffusion model fitting results (Figure 2b, Table S2) showed that the fitted lines for the diffusion stage did not pass through the origin, indicating that both surface adsorption and intra-particle diffusion controlled the adsorption rate [26]. The larger intercept for RHB600 compared to RHB400 and RHB500 suggests a greater contribution from surface adsorption, consistent with its richer surface functional group structure. The multi-linearity in the intra-particle diffusion plot is frequently observed and suggests that adsorption occurs through a multi-step process, starting with boundary layer diffusion and followed by intra-particle diffusion, which is a common pattern in porous biochar adsorbents [51].

3.3. Analysis of Isothermal Adsorption Results

3.3.1. Adsorption Isotherm

The adsorption isotherms of DIN on RHBs are shown in Figure 2c. The adsorption capacity increased rapidly at low DIN concentrations and gradually approached saturation as the equilibrium concentration rose. Within the tested concentration range, RHB600 exhibited a significantly higher adsorption capacity for DIN than RHB400 and RHB500.

This enhancement is primarily attributable to its superior SSA and more developed pore structure resulting from higher pyrolysis temperature, a trend well-documented for the thermal activation of biochars [24]. As surface area significantly influences adsorbent performance, the adsorption capacity was normalized by the SSA (Figure S4a). The non-overlapping trends after normalization demonstrated that SSA was not the primary factor causing the differences in DIN adsorption [51]. Other factors, such as pore structure and surface functional groups, played more critical roles. This finding is consistent with studies on other contaminants, which suggest that once a certain SSA threshold is met, surface chemistry and pore architecture become the dominant factors governing adsorption capacity [29,51].

The Langmuir, Freundlich, and Sips models were applied to analyze the adsorption behavior and mechanism. Both the Langmuir (R^2: 0.9649–0.9868) and Freundlich (R^2: 0.9827–0.9894) models provided reasonably good fits (Table S3), suggesting that both monolayer and multilayer adsorption could partially describe the process [39]. However, due to the idealized assumptions of these models, the Sips model, a hybrid isotherm, yielded the best fit (R^2: 0.9932–0.9977) for this heterogeneous system [32]. The deviation of the Sips parameter m from 1 indicated the presence of heterogeneous adsorption sites on the RHB surface [32,39]. The m value for RHB600 was closer to 1 than those for RHB400 and RHB500, suggesting that higher pyrolysis temperature increased the homogeneity of the active adsorption sites [32,39]. To contextualize the performance of our materials, the maximum adsorption capacity (Q_m) of RHB600 for DIN, as derived from the Sips model (49.73 mg/g), compares very favorably with other adsorbents reported in recent literature (Table S4). For instance, RHB600′s capacity is substantially higher than that of biochar-based composites like a magnesium oxide-biochar composite (2.18 mg/g) [27], and vastly outperforms common minerals such as montmorillonite (2.28 mg/g) and kaolinite (0.39 mg/g) [52]. This superior performance of a relatively unmodified rice husk biochar underscores the inherent suitability of rice husk as a precursor for creating high-capacity adsorbents for DIN, likely due to its unique combination of organic carbon and inorganic silica.

3.3.2. Site Energy Distribution Theory

The Sips model was specifically selected as the basis for the site energy distribution (SED) analysis due to its superior ability to characterize heterogeneous adsorption systems. While the Langmuir model assumes a uniform surface with identical adsorption sites, and the Freundlich model is an empirical equation for heterogeneous surfaces without a theoretical saturation limit, the Sips model serves as a hybrid that combines their advantages. It not only predicts a monolayer saturation capacity (Q_m) but also introduces a heterogeneity parameter (m), which quantitatively describes the deviation from an ideal homogeneous surface. The mathematical form of the Sips isotherm can be directly derived from and is fundamentally linked to the concept of a quasi-Gaussian energy distribution, making it a theoretically sound foundation for subsequent SED analysis [32,39].

Furthermore, the Sips model was linked to the SED theory, relating the macroscopic adsorption process to adsorption energy [32,39]. Assuming the RHB surface possesses adsorption sites characterized by a heterogeneous energy distribution, the relationship between the energy distribution and the residual DIN concentration (C_e) can be expressed by Equation (2):

$$C_e = C_s exp\left[\frac{-(E - E_s)}{RT}\right] = C_s \exp\left(-\frac{E^*}{RT}\right) \tag{2}$$

where C_s (mg/L) is the maximum solubility of DIN, R is the ideal gas constant (0.008314 kJ/mol/K), T is the Kelvin temperature (K), E (kJ/mol) and E_s (kJ/mol) represent the thermodynamic potential energy at DIN concentrations of C_e and C_s, respectively. Therefore, the potential energy difference is $E^* = E - E_s$.

Therefore, for heterogeneous adsorbent RHB, the relationship between the adsorption capacity Q_e of DIN and the adsorption potential energy can be expressed by Equations (3) and (4):

$$Q_e(C_e) = \int_0^{+\infty} F(E^*)\, dE^* \tag{3}$$

$$F(E^*) = \frac{-dQ_e(E^*)}{dE^*} \tag{4}$$

Therefore, the energy distribution function F (E^*) derived from the Sips model can be expressed as Equations (5) and (6) [32,39]:

$$F(E^*) = Q_m \cdot \frac{(K_S C_e)^{1/m} \cdot \exp\left(-\frac{E}{mRT}\right)}{mRT\left[1 + (K_S C_e)^{1/m} \cdot \exp\left(\frac{E}{mRT}\right)\right]^2} \tag{5}$$

$$E_m^* = RTln(k_s C_s) \tag{6}$$

K_s and m are parameters in the Sips model, and the characteristic energy E_m* (kJ/mol) corresponds to the critical point of the energy distribution, where $E^* < E_m^*$ is the low-energy adsorption site, and vice versa is the high-energy adsorption site ($E^* > E_m^*$) [41].

The quasi-Gaussian properties of the F (E^*) function indicate that its weighted average (μ, Equations (7) and (8)) can be used to represent the adsorption affinity between RHB and DIN, while the standard deviation (σ, Equation (9)) can be used to evaluate the uniformity of RHB surface composition [28]. The higher the μ value, the stronger the adsorption affinity between the two, and the smaller the σ value, the more uniform the surface energy distribution of RHB.

$$\mu\ (E^*) = \frac{\int_{E*}^{+\infty} E^* F(E^*) \mathrm{d}E^*}{\int_{E*}^{+\infty} F(E^*) \mathrm{d}E^*} \tag{7}$$

$$\mu\ (E^{*2}) = \frac{\int_{E*}^{+\infty} E^{*2} F(E^*) \mathrm{d}E^*}{\int_{E*}^{+\infty} F(E^*) \mathrm{d}E^*} \tag{8}$$

$$\sigma_e^* = \sqrt{\mu(E^{*2}) - \mu(E^*)^2} \tag{9}$$

The SED profiles for DIN adsorption on RHBs, derived from the Sips model, are shown in Figures 2d and S4b. Figure S4b shows that the adsorption energy decreased rapidly with increasing adsorption capacity for all RHBs. This inverse relationship indicates that DIN molecules preferentially occupied high-energy sites before adsorbing onto lower-energy sites [32,39].

Furthermore, RHB600 showed a larger σ_e* value from the SED function compared to RHB400 and RHB500 (Figure 2d), indicating stronger energy heterogeneity for the latter two [26]. This is attributed to their greater abundance of surface functional groups and lower aromaticity. The mean site energy, $\mu(E^*)$, was higher for RHB600, indicating a stronger overall adsorption affinity for DIN. This benefits from RHB600′s more developed microporous structure and oxygen-containing functional groups, enhancing pore-filling and hydrogen bonding interactions [26,53].

It is noteworthy that the maximum adsorption capacity of RHB600 for DIN compares favorably with a wide range of other adsorbents reported in the literature, as summarized in Table S4. The adsorption capacities of common minerals, such as clay or Kaolin, were lower than that of RHB. Some microplastics and wood-based biochar also have less ideal adsorption effect on DIN than RHB. This positions RHB600, derived from abundant agricultural waste, as a highly competitive material for practical applications. Overall, RHB600 is a more suitable candidate for removing DIN from aqueous solutions and was therefore selected for further investigation into the effects of environmental factors.

3.4. Adsorption Thermodynamics

The adsorption of DIN on RHB600 was investigated at three common environmental temperatures (288.15 K, 298.15 K, and 308.15 K). The results indicated that the adsorption capacity of RHB600 for DIN gradually increased with rising temperature (Figure S5), suggesting that elevated temperature activated more adsorption sites. The thermodynamic parameters are listed in Table S5. The negative value of the Gibbs free energy change (ΔG) across all temperatures confirmed the spontaneity of the adsorption process, and the decrease in its value with increasing temperature indicated enhanced spontaneity at higher temperatures [51]. The positive enthalpy change (ΔH) revealed the endothermic nature of the adsorption. The magnitude of ΔH (less than 20 kJ/mol) is consistent with a physisorption-dominated process, which may involve forces such as van der Waals interactions, pore filling, and weak hydrogen bonding [54]. The positive entropy change (ΔS) suggests an increase in the overall disorder of the system. This can be attributed to the release of bound water molecules from the surfaces of both RHB600 and DIN upon adsorption, as well as an increased freedom of the adsorbed species at the solid–liquid interface.

The SED analysis, derived from the Sips model, provides a complementary, microscopic perspective on the adsorption energy landscape under different temperatures. It is important to distinguish these SED-derived energy values (E, E_{m}) from the macroscopic thermodynamic parameters; the former describe the energy heterogeneity of specific adsorption sites, while the latter reflect the net energy change of the entire bulk system. The SED analysis showed a rapid decrease in adsorption energy with increasing adsorption capacity (Figure 3a), indicating that higher-energy sites are occupied first. The fact that the overall energy distribution shifted towards higher values with increasing temperature (Figure 3b, Table S6) suggests that a greater proportion of adsorption sites became accessible and effective, which may be due to enhanced molecular diffusion and a higher probability of overcoming energy barriers at elevated temperatures. This is because higher temperature reduces the viscosity of the solution, decreasing diffusion resistance at the solid–liquid boundary and facilitating faster binding of DIN to RHB600 [28]. The characteristic energy, E_m*, increased from 18.24 kJ/mol at 288.15 K to 22.38 kJ/mol at 308.15 K, reflecting this shift in the energy profile [32,39]. The increase in the mean site energy, $\mu(E^*)$, with temperature further confirms the enhanced affinity between RHB600 and DIN.

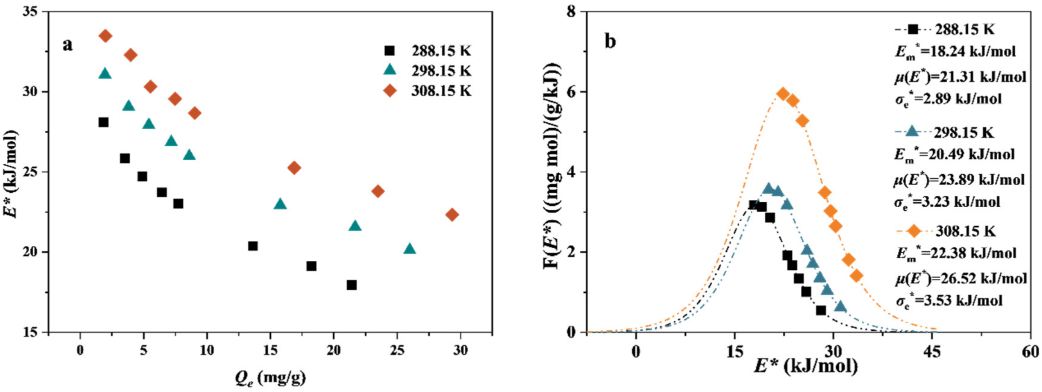

Figure 3. (**a**) Site adsorption energy (E*) against DIN adsorption capacity of RHB600, and (**b**) site energy distribution of RHB600 at different temperatures.

3.5. Influence of Individual Environmental Factors

3.5.1. Ionic Strength

The effect of ionic strength on DIN adsorption by RHB600 was generally not significant (Figure S6a). When the ionic strength increased from 0 to 1 mM, the adsorption capacity of DIN increased by 0.61 mg/g. However, a further increase to 20 mM led to a decrease of 2.53 mg/g. This suggests that low ionic strength can promote DIN adsorption, primarily because Na^+ ions neutralize some negative charges on the RHB600 surface and compress the electrical double layer, thereby reducing electrostatic repulsion between RHB600 and DIN [26,53]. At higher ionic strengths (>10 mM), Na^+ ions form weak electrostatic interactions with the RHB600 surface, which weakens hydrogen bonding between DIN and the polar functional groups on the biochar surface [27]. Additionally, Na^+ ions and their associated water clusters can occupy some adsorption sites, leading to a decrease in DIN adsorption [55].

3.5.2. Adsorbent Dosage

The dosage of RHB600 significantly influenced DIN removal (Figure 4a). At lower dosages (<0.02 g in this study), the adsorption capacity of DIN increased with the RHB600 dose because DIN was in excess and could fully occupy the available adsorption sites [39]. Since the initial DIN concentration was fixed, adding more than 0.02 g of RHB600 provided abundant total adsorption sites, sufficient to accommodate all DIN molecules in the system. This resulted in underutilization of some sites and a consequent decrease in the apparent adsorption capacity [56]. The DIN removal efficiency increased from 46.30% to 77.19% as the RHB600 dosage rose from 0.01 g to 0.02 g. Further increases in dosage did not significantly improve removal efficiency. Therefore, a dosage of 0.02 g was identified as optimal for this system.

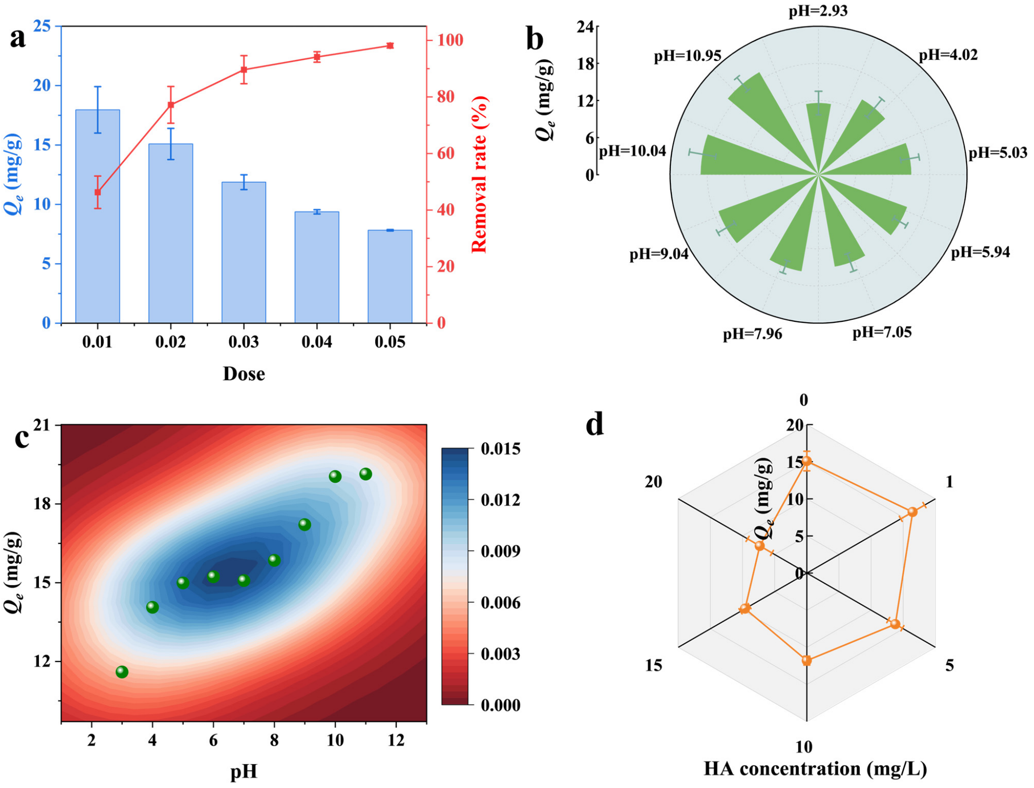

Figure 4. Effects of (**a**) dose, (**b**) initial pH value on DIN adsorption by RHB600. (**c**) Scatter kernel density diagram of RHB600. (**d**) Effects of HA concentration on DIN adsorption by RHB600.

3.5.3. Solution pH

Solution pH is a key factor affecting adsorption, as it influences both the speciation of DIN and the surface charge/functionality of RHB600. The adsorption capacity of DIN on RHB600 increased with rising initial pH (Figure 4b, Q_e from 12.60 mg/g to 20.14 mg/g), and good performance was maintained over a wide pH range. The kernel density distribution of Q_e under different pH conditions showed an overall increasing trend, with the highest density area concentrated between pH 5.5 and 7.5 (Figure 4c). As shown in Figure S7a, DIN exists predominantly in its neutral or inner salt form ($DIN^{\pm}$) at pH > 3.0. Within this pH range, the RHB600 surface is negatively charged (Figure S7b, Table S7). Therefore, electrostatic interaction was not the driving force for adsorption [27,56]. The increase in pH promotes the deprotonation of functional groups like Si-OH and C-OH on RHB600, which can form hydrogen bonds with –NH and –CONH– groups in DIN molecules, thereby enhancing adsorption [26]. The π–π interactions between the aromatic moieties of RHB600 and DIN are relatively insensitive to pH changes [26]. Furthermore, the solvent layer on the RHB600 surface becomes thinner under alkaline conditions, potentially enhancing pore-filling and hydrophobic effects.

3.5.4. HA Concentration

The concentration of HA in the system significantly altered the adsorption capacity (Figure 4d). A low HA concentration (1 mg/L) increased DIN removal by 9.04%. At this level, HA molecules initially adsorb onto RHB600, forming a sparse organic coating [26]. The aromatic fragments and polar groups of HA provide additional π-systems and hydrogen bonding sites on the RHB600 surface and pores, potentially enhancing DIN adsorption. Simultaneously, low-concentration HA does not fully occupy the adsorption sites, resulting in weak competition with DIN [27]. These combined effects lead to the observed increase. In contrast, high concentrations of HA significantly inhibited DIN removal ($p < 0.05$), with reduction rates ranging from 8.76% to 51.54%. This is because excessive HA molecules coat the RHB600 surface, blocking most adsorption sites and drastically reducing access for DIN [27]. Additionally, HA in solution can bind with free DIN molecules, hindering their diffusion into RHB600 micropores or formation of hydrogen bonds, thus severely suppressing adsorption.

3.5.5. Co-Existing Anions

Wastewater or environmental waters often contain various anions (e.g., NO_3^-, PO_4^{3-}, Cl^-, SO_4^{2-}), which may interfere with DIN adsorption. As shown in Figure S6b, NO_3^-, Cl^-, and SO_4^{2-} had no significant effect ($p > 0.05$), whereas PO_4^{3-} significantly inhibited adsorption ($p < 0.05$). This is because PO_4^{3-} competes with DIN for the same adsorption sites. This is because PO_4^{3-}, a common oxyanion in aquatic environments, competes with DIN for the specific adsorption sites on the biochar surface, a phenomenon well-documented for phosphate on engineered and waste-derived adsorbents [57]. Chen et al. reported a strong affinity of biochar for phosphate [58]. The adsorption of PO_4^{3-} onto RHB600 blocks a portion of the sites, reducing the capacity for DIN. Thus, PO_4^{3-} can significantly inhibit DIN adsorption via competitive adsorption. Typical phosphate concentrations in freshwater systems range from 0.01 to 2 mg/L, while wastewater can contain 2–10 mg/L PO_4^{3-} [59]. At environmentally relevant concentrations (<1 mg/L), the inhibitory effect would be moderate, but in phosphate-rich wastewater (>5 mg/L), significant inhibition (up to 40%) may occur, requiring dosage adjustment in practical applications. In contrast, NO_3^-, Cl^-, and SO_4^{2-} primarily form weak electrostatic interactions or occupy weak adsorption sites on the RHB600 surface, resulting in negligible inhibition [27]. Their typical environmental concentrations (NO_3^-: 0.1–50 mg/L; Cl^-: 1–200 mg/L; SO_4^{2-}: 2–200 mg/L) [60] do not substantially compromise DIN removal by RHB600, highlighting the material's selectivity in complex water matrices.

3.5.6. Co-Existing Cations

The presence of cations with different valences (Na^+, K^+, Ca^{2+}, Fe^{3+}) in the solution can also affect DIN adsorption (Figure S6c). Monovalent cations showed no significant influence ($p > 0.05$), due to their low charge density and stronger interaction with water molecules than with the RHB600 surface. Both Ca^{2+} and Fe^{3+} significantly enhanced DIN adsorption ($p < 0.05$), increasing the adsorption capacity by 12.27% and 19.76%, respectively. This suggests that di- and trivalent cations enhance the interaction between RHB600 and DIN via cation-bridging, where the cation forms complexes with both the negatively charged biochar surface and the polar groups of DIN [61]. Compared to Ca^{2+}, Fe^{3+} exhibits stronger bridging ability due to its higher charge density and Lewis acidity, enabling more effective coordination with both adsorbent and adsorbate [27]. Furthermore, Fe^{3+} can hydrolyze in solution to form $Fe(OH)_x$ polymers, providing new metal oxide surfaces for adsorption, thereby significantly increasing the adsorption capacity [62]. These hydrolysis products can adsorb onto the RHB600 surface, creating new iron (hydr)oxide interfaces with high affinity for DIN molecules through ligand exchange and surface complexation mechanisms [63]. Thus, according to the results of this experiment, at environmentally relevant Fe^{3+} levels (<1 mg/L), DIN adsorption would increase by approximately 5–8%, while in iron-rich groundwater or acid mine drainage, enhancement could exceed 15%.

3.6. Interactive Effects of Combined Environmental Factors

3.6.1. RSM Analysis

Table S8 presents the matrix of variables from the Central Composite Design (CCD), the experimental values of DIN removal efficiency, and the corresponding predicted values from the RSM model. Based on the experimental results from this design matrix, an empirical model function for the response surface was obtained (Equation (10)). This equation describes the nonlinear relationship between the three variables and DIN removal efficiency [29]. Additionally, the associated Analysis of Variance (ANOVA) information is listed in Table S9. The RSM model achieved an R^2 value of 0.9790, indicating its high accuracy in predicting DIN removal by RHB600. The model's high F-value (118.74) and significant p-value (<0.0001) confirm its statistical significance for simulating the adsorption process.

$$\begin{gathered} y = 59.2 - 9.64x_1 + 3.55x_2 - 1.24x_3 - 0.6024{x_1}^2 + 0.1826{x_2}^2 - 0.0755{x_3}^2 + \\ 0.4506x_1x_2 - 0.4975x_1x_3 - 0.1519x_2x_3 - 0.0475x_1x_2x_3 \end{gathered} \quad (10)$$

The RSM analysis revealed that the adsorption of DIN onto RHB600 was significantly influenced by the synergistic effects of solution pH and HA concentration, while the interaction with ionic strength was relatively weaker (Figure 5 and Figure S8). These results reflect the varying roles of electrostatic interactions and surface complexation under different pH conditions. At lower pH, the RHB600 surface bears protonated functional groups (e.g., –COOH, –OH), facilitating electrostatic attraction and hydrogen bonding with amino or carbonyl groups in DIN [35]. As pH increases, surface deprotonation leads to negatively charged sites. HA molecules, containing abundant carboxylic and phenolic hydroxyl groups, compete with DIN for adsorption sites or form soluble complexes, reducing the effective DIN concentration in solution [18]. Thus, higher HA concentrations generally inhibit adsorption. The influence of ionic strength primarily involves charge shielding [61]. A moderate increase can promote ion redistribution and reduce surface potential barriers, enhancing adsorption within a certain range [64]. However, excessively high ionic strength compresses the electrical double layer and weaken the driving force of adsorption [55].

Overall, the RSM model effectively elucidated the multi-factor interactions governing DIN adsorption on RHB600.

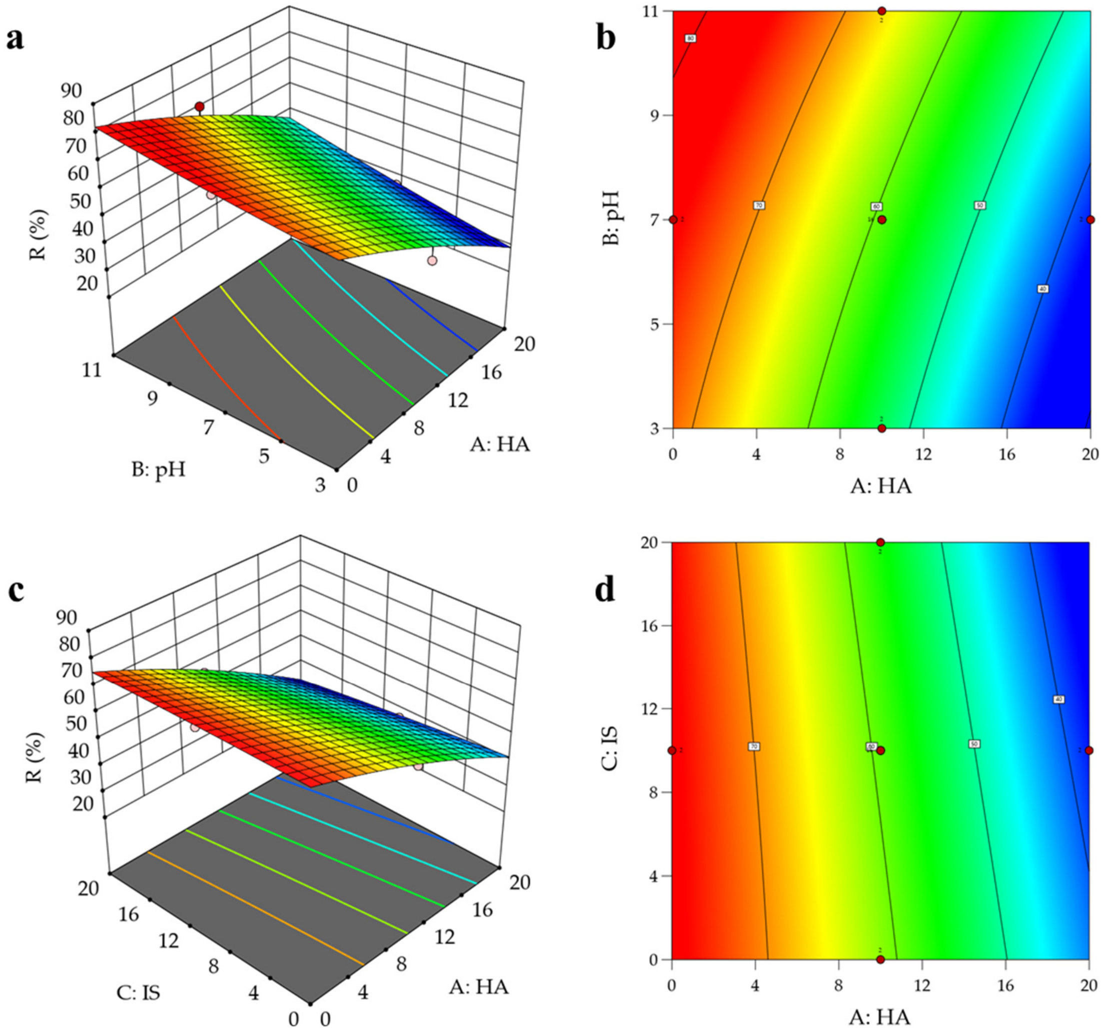

Figure 5. Effect of solution pH–HA–IS concentration on adsorption capacity of RHB600: (**a**,**c**) the response surface diagram of RHB600, (**b**,**d**) the contour map of RHB600.

3.6.2. ANN Analysis

The experimental dataset was divided into 70% for training, 15% for testing, and 15% for validation to enhance the reliability and generalizability of the ANN model. A suitable ANN topology was established after 5 iterative training (Figure S9). Figure 6 shows that the correlation coefficients (R) for the training, testing, and validation phases of the ANN model all exceeded 0.99, indicating a highly satisfactory response of this topology for predicting RHB600 adsorption [29]. The predicted DIN removal efficiencies under the trained ANN topology showed excellent agreement with the experimental values, demonstrating the model’s capability for predicting removal efficiency under specific conditions of pH, ionic strength, and HA concentration.

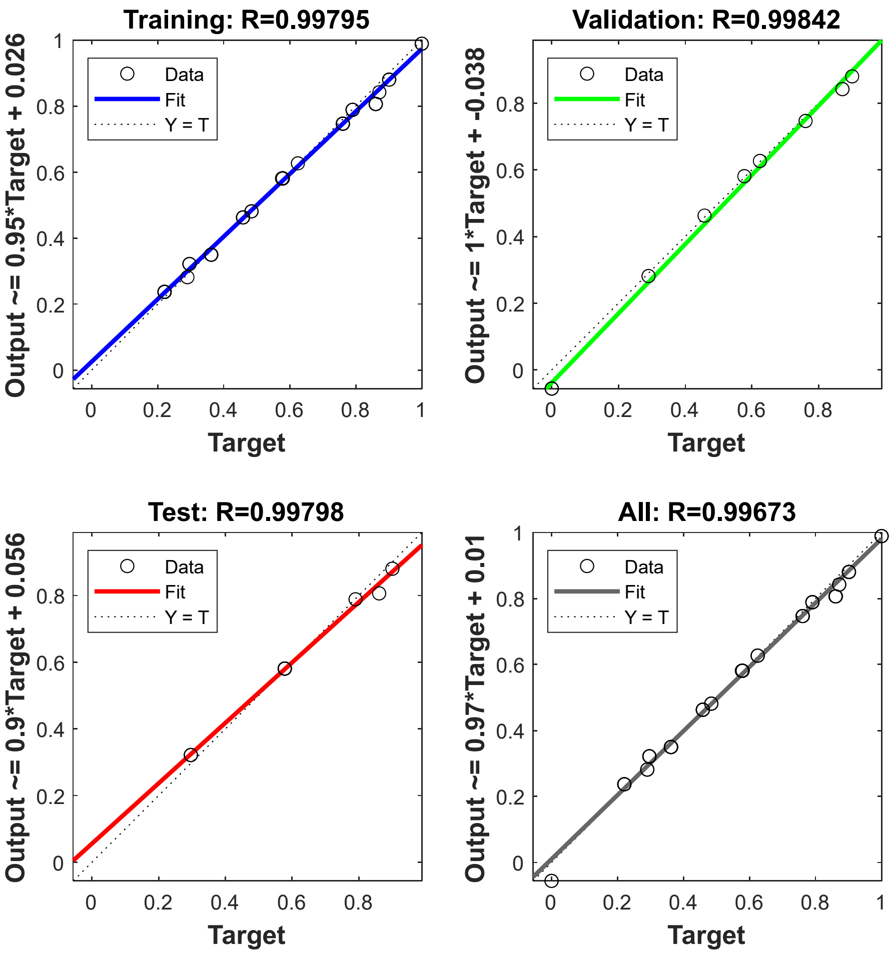

Figure 6. Regression plot for training data, validation data, testing data, and overall data.

3.6.3. Comparison and Validation of RSM and ANN

Both RSM and ANN are excellent models for handling linear and nonlinear multivariate relationships [65]. Both models produced predicted values for DIN removal by RHB600 that closely matched the experimental data (Table S8). The RSM model offers a regression equation (Equation (10)), which is useful for prediction and determining optimal conditions. However, a key limitation of RSM is its restriction to second-order nonlinearities [66]. In contrast, the ANN model can handle nonlinearities of any form [65]. The performance of both models was evaluated using the sum of squared errors (*SSE*), mean squared error (*MSE*), average relative error (*ARE*), and coefficient of determination (R^2), calculated via Equations (11)–(14) [65,66]. Table 2 lists the R^2, *MSE*, *SSE*, and *ARE* values for both the training and checking sets of RSM and ANN. The results show that the ANN model outperformed the RSM model across these metrics. Therefore, the ANN demonstrated superior accuracy and predictability compared to RSM for forecasting DIN removal by RHB600.

$$SSE = \sqrt{\frac{\sum_{i=1}^{N}\left(y_{i,exp} - y_{i,pred}\right)^2}{N}} \tag{11}$$

$$MSE = \frac{1}{N}\sum_{i=1}^{N}\left(y_{i,pred} - y_{i,exp}\right)^2 \tag{12}$$

$$ARE = \frac{100}{N}\sum_{i=1}^{N}\left|\frac{y_{i,pred} - y_{i,exp}}{y_{i,exp}}\right|\% \tag{13}$$

$$R^2 = 1 - \sum_{i=1}^{N} \left(\frac{\left(y_{i,pred} - y_{i,exp}\right)^2}{\left(y_{avg,exp} - y_{i,exp}\right)^2} \right) \quad (14)$$

where N is the number of experimental data, $y_{i,pred}$ and $y_{i,exp}$ are the predicted and experimental values, respectively. $y_{avg,exp}$ is the average of experimental values.

Table 2. Error rates of the RSM and ANN prediction models.

Index	RSM		ANN	
	Training	Checking	Training	Checking
R^2	0.9751	0.9908	0.9916	0.9942
MSE	2.3492	0.6842	0.7867	0.4341
SSE	1.5327	0.8272	0.8870	0.6589
ARE	1.9539	1.2760	1.1096	0.7652

3.7. Reusability of RHB600

The reusability and stability of an adsorbent are crucial metrics for assessing its commercial potential. After five adsorption–desorption cycles, ethanol recovered 55% of the initial adsorption capacity of RHB600, while HCl and NaOH recovered 38% and 40%, respectively (Figure S10). Ethanol was significantly more effective as a desorbing agent than HCl or NaOH. This is because DIN adsorption on RHB600 relies primarily on reversible weak interactions such as hydrophobic effects, π–π interactions, and hydrogen bonding [26,27]. Ethanol alters the solvation structure and reduces the dielectric constant of the polar solvent, facilitating DIN desorption from the pores and surface of RHB600 without causing severe corrosion or altering its surface structure significantly [67]. HCl protonates the oxygen-containing groups on RHB600 and may leach soluble metals from the ash, reducing hydrogen bonding or Lewis basic sites [13]. NaOH may etch the silicon skeleton of RHB600 or enhance surface deprotonation, introducing a thicker hydration layer [35]. This can lead to reduced pore size in subsequent adsorption cycles and lower affinity between DIN and the RHB600 interface. Furthermore, HCl and NaOH treatments may strip weakly bound aromatic fragments from RHB600, diminishing its capacity for π–π interactions with DIN.

Despite ethanol being the most effective desorbent, the gradual decline in adsorption capacity to 55% after five cycles indicates some irreversible processes occurring during repeated use. The performance loss could be attributed to several factors. First, irreversible pore blockage might occur, where a fraction of the DIN molecules or their transformation products, as well as potential humic acid residues from the environmental factor experiments, become strongly trapped within the micropores of RHB600, thereby reducing the accessible surface area and pore volume for subsequent adsorption cycles [26]. Second, although ethanol is relatively mild, cumulative surface chemical alteration cannot be entirely ruled out. This may include the irreversible binding of DIN to high-energy sites or slight changes in the surface functional groups that are critical for hydrogen bonding and π–π electron donor-acceptor interactions [26,27]. To mitigate this performance loss in future applications, strategies such as employing a sequential wash with ethanol followed by a milder solvent to flush out trapped residues, or implementing a low-temperature thermal regeneration process in an inert atmosphere to decompose stubborn contaminants without damaging the biochar structure, could be explored.

3.8. Adsorption Mechanism

The FTIR spectra of RHB600 after adsorption of DIN at different initial concentrations (0–40 mg L^{-1}) are shown in Figure S11. The intensities of the O–H stretching broad band (3000–3700 cm^{-1}), the C=O/C=N region (1680–1800 cm^{-1}), the aromatic C=C (1580–1660 cm^{-1}), C–O (phenolic hydroxyl/ether, 1200–1270 cm^{-1}), Si–O–Si (1000–1160 cm^{-1}), and Si–OH (930–965 cm^{-1}) all increased with rising DIN concentration. Bands directly associated with DIN functional groups also showed synchronous enhancement. For instance, the peak intensities for NO_2 asymmetric stretching (1535–1560 cm^{-1}) and symmetric stretching (1330–1370 cm^{-1}) increased by 20.7% and 21.8%, respectively, and the C–N peak (1215–1245 cm^{-1}) intensity increased by 21.4%. These results confirm the enrichment of DIN molecules on the surface and within the pores of RHB600 [53]. The 2D-COS synchronous spectrum (Figure 7a) showed predominantly positive cross-peaks between the aforementioned bands, indicating their synchronous and concerted changes with increasing DIN concentration [49]. The asynchronous spectrum (Figure 7b) revealed the sequential response of key bands of RHB600. The C–O (1250 cm^{-1}) and Si–O–Si (1100 cm^{-1}) responded first (C–O slightly preceding Si–O–Si), followed by the aromatic C=C (1600 cm^{-1}). The response of C=O/C=N (1720 cm^{-1}) was slower, while the -OH response was the last. Comparison with DIN fingerprint bands showed that the response of the NO_2 group at 1350 cm^{-1} lagged behind those at 1720 cm^{-1} and 1600 cm^{-1}, suggesting its spectral changes correspond to later-stage conformational adjustments [43,49].

This sequence of functional group response provides direct, time-resolved evidence for the adsorption mechanism. The earliest response of C–O and Si–O–Si groups signifies that they serve as the primary active sites for the initial anchoring of DIN molecules through hydrogen bonding and Lewis acid-base interactions [49]. Specifically, the C–O groups (e.g., phenolic –OH, ether) act as hydrogen bond donors/acceptors, while the siloxane network (Si–O–Si/Si–OH) provides Lewis acid-base interaction sites, facilitating the “initial anchoring” of DIN. The subsequent response of aromatic C=C confirms the synergistic role of π–π interactions in stabilizing the adsorbed DIN, particularly within the hydrophobic microporous structure of RHB600 [26,27]. The delayed enhancements of C=O/C=N and O–H bands suggest a later-stage strengthening of hydrogen bonds and a rearrangement of the hydrogen-bonding network after the initial adsorption.

At low DIN concentrations, the oxygen-containing groups (C–O) and the mineral siloxane network (Si–O–Si/Si–OH) on the RHB600 surface changed first. This indicates that DIN initially anchors to polar sites and the amorphous silica-ash interface via hydrogen bonding, Lewis acid-base, and charge-assisted interactions [24,49]. The preferential response of C–O suggests that phenolic hydroxyl/ether bonds are crucial for initial DIN adsorption and reducing diffusion barriers [43,49]. The earlier response of aromatic C=C compared to C=O/C=N indicates that π–π/π–π^* interactions contribute synergistically to the hydrophobic partitioning and pore stabilization of DIN [26]. The subsequent enhancement of C=O/C=N reflects stronger hydrogen bonding and charge transfer between the adsorbed DIN molecules and the –OH/C–O sites on the RHB600 [26,27]. The delayed response of O–H is consistent with the sequence of related cross-peaks (1720 cm^{-1}→3400 cm^{-1}, 1100 cm^{-1}→3400 cm^{-1}), implying a lagged rearrangement of the hydrogen-bonding network after DIN occupies the adsorption sites [27,49]. This arises from both the re-coordination of –OH groups on RHB600 and an increase in bound water molecules around the adsorbed DIN.

The XPS results of RHB600 before and after DIN adsorption are shown in Figure 7c–f. In the C1s spectrum (Figure 7c,e), characteristic peaks for C–C/C=C, C–O, and O–C=O appeared at 284.7 eV, 285.5 eV, and 288.6 eV, respectively. After DIN adsorption, the O-C=O peak shifted to 288.2 eV. Furthermore, new peaks appeared at 286.7 eV and 290.8 eV, corresponding to C=N and C-N, confirming the adsorption of DIN molecules on the RHB600 surface [49]. In the O1s spectrum (Figure 7d,f), the peaks for C=O and O–H shifted from 531.7 eV and 534.9 eV to 531.8 eV and 535.2 eV, respectively. After DIN adsorption, the formation of hydrogen bonds and Lewis acid-base interactions between the C–O groups of RHB600 and the C=O/C–N groups of DIN led to an increased contribution of C–O/C–N, C=O, and O–C=O in the C1s spectrum, accompanied by a slight shift in binding energy [43,49]. The synchronous enhancement of C=O and C–O in the O1s spectrum indicates the participation of inorganic ash components and oxygenated sites in coordination and hydrogen bonding. The core peak for C–O at 533.5 eV showed no significant shift, suggesting that DIN adsorption primarily involves multisite non-covalent binding and pore-filling [43,49].

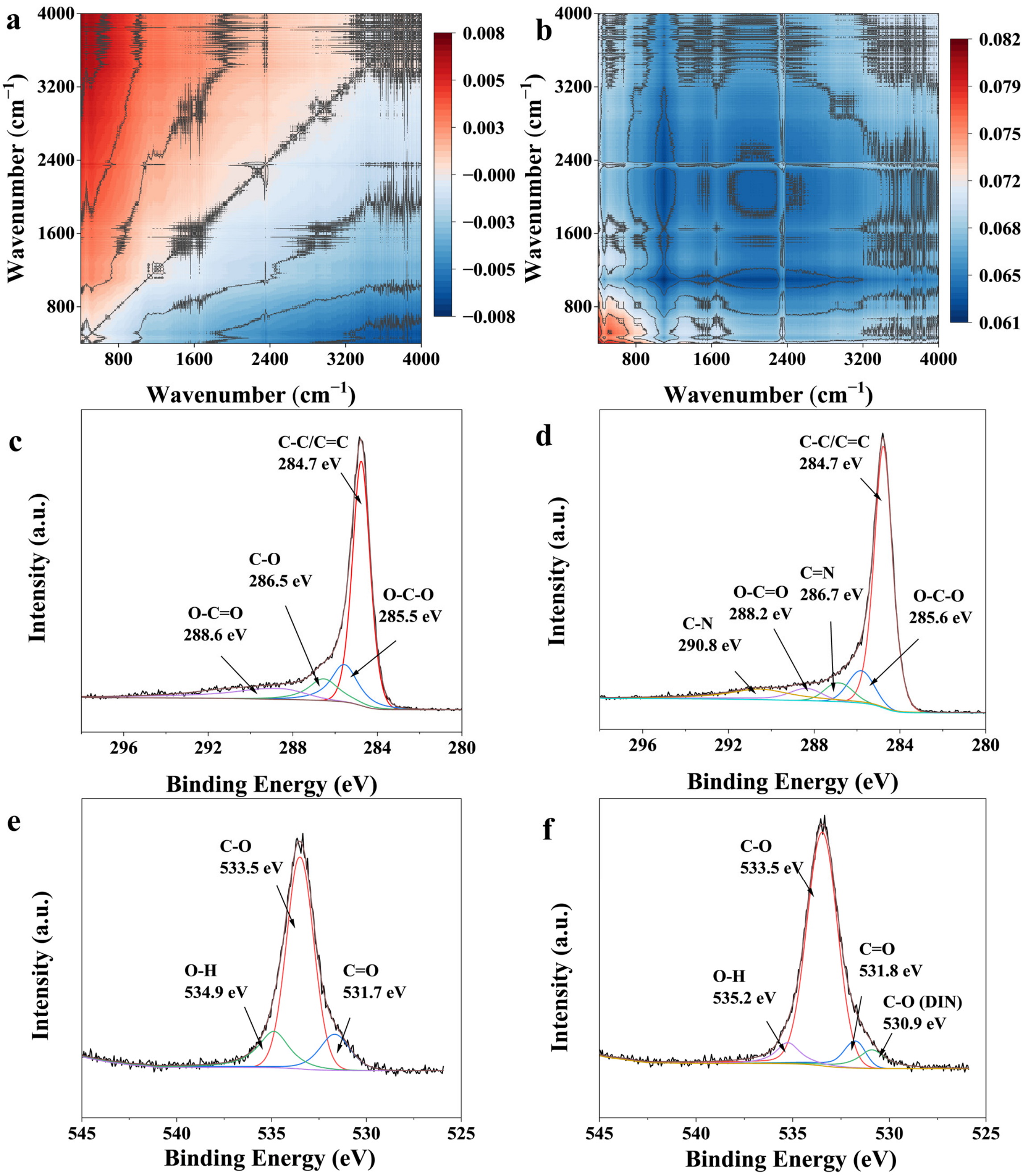

Figure 7. Adsorption behavior and changes in RHB600 after DIN adsorption. (**a**) Synchronous spectrum and (**b**) asynchronous spectrum generated from FTIR analysis of RHB600 with DIN (0–40 mg/L) binding in the region of 400–4000 cm^{-1}. XPS spectra of C and O elements in RHB600 (**c**,**e**) before and (**d**,**f**) after DIN adsorption.

To further understand the adsorption mode, electrostatic potential (ESP) analysis was conducted for RHB600 and DIN (Figure 8). The positively charged hydrogen atoms of

–OH/–COOH groups at the edges of RHB600 form strong directional hydrogen bonds with the negatively charged regions of the NO_2–O and carbonyl oxygen of DIN [26,68]. Conversely, the negatively charged regions of C=O/C–O–C on RHB600 act as hydrogen bond acceptors, complementarily coordinating with the –NH and positively charged C=N groups of DIN [26]. This explains the preferential response of C–O and Si–O–Si in 2D-COS and the slight positive shifts of C–O/C=O in XPS. The continuous, weakly polar, negatively charged aromatic basal planes of RHB600 readily engage in π–π interactions with the furan/aromatic heterocycles of DIN [26,43]. This provides a stable internal structure and facilitates pore allocation for DIN adsorption.

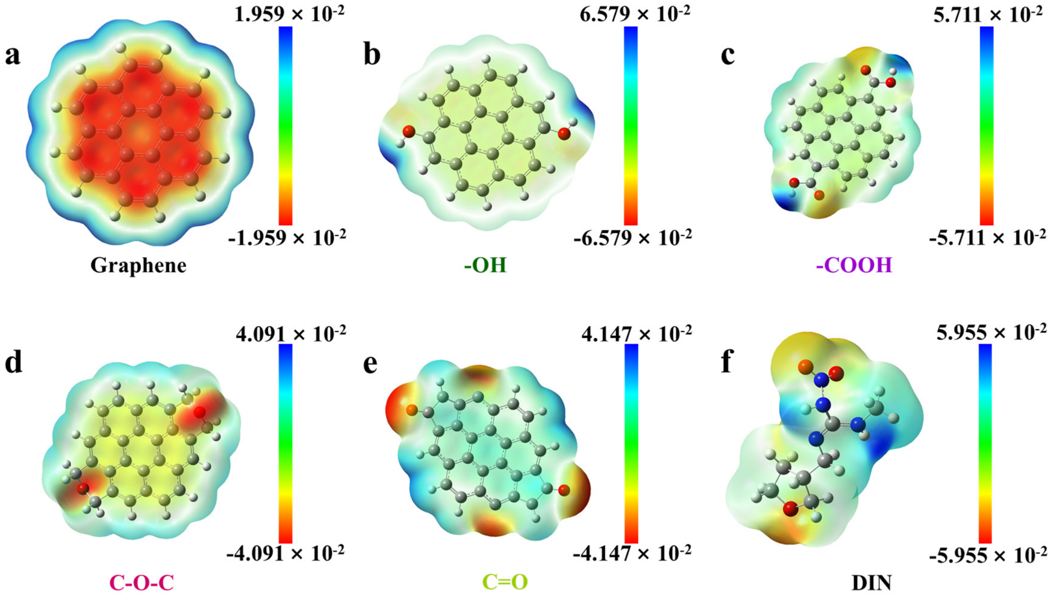

Figure 8. (**a**–**f**) Mapping of the electrostatic potential on electron isopycnic surface. The gray atom is carbon, the white atom is hydrogen and the red atom is oxygen. The blue area reflects the positive polarity, whereas the red reflects the negative polarity.

The synergistic adsorption mechanisms of DIN on RHB600, as elucidated by the combined evidence from FTIR, 2D-COS, XPS, and DFT analysis, are summarized in Table 3. This table provides a concise correlation between each proposed mechanism—namely, pore filling, π–π interactions, hydrogen bonding, and Lewis acid-base interactions—and the specific experimental observations that support them. Collectively, the data supports a multi-step adsorption process: DIN is initially anchored to polar C–O and Si–O–Si sites via hydrogen bonding, as indicated by their prior response in the 2D-COS analysis; subsequently, the molecule is stabilized through π–π interactions with the aromatic biochar matrix and further entrenched within the micropores via pore-filling.

Table 3. Summary of proposed adsorption mechanisms and corresponding experimental evidence.

Proposed Mechanism	Experimental Evidence	Key Observations and Interpretation
Pore Filling	SSA Analysis	Increase in SSA and microporosity with pyrolysis temperature (RHB400 to RHB600) correlates with enhanced adsorption capacity.
	Adsorption Kinetics	The intra-particle diffusion model indicates that pore diffusion is a rate-controlling step.

Table 3. *Cont.*

Proposed Mechanism	Experimental Evidence	Key Observations and Interpretation
π–π Interaction	FTIR & 2D-COS	Enhancement of aromatic C=C (1600 cm^{-1}) band; Its response after C–O in 2D-COS suggests a synergistic role following initial anchoring.
	XPS	Appearance of new C=N and C–N peaks in the C1s spectrum after adsorption, confirming the proximity of DIN's aromatic rings to the biochar surface.
	DFT (ESP Analysis)	Complementary negative ESP regions on RHB600′s aromatic basal planes and DIN's furan ring facilitate electron donor-acceptor interactions.
Hydrogen Bonding	FTIR & 2D-COS	Synchronous increase in O–H, C=O, C–O bands with DIN concentration; The earliest response of C–O and Si–O–Si in 2D-COS identifies them as key initial hydrogen-binding sites.
	XPS	Shifts in the binding energy of O–C=O (C1s) and O–H (O1s) peaks after adsorption, indicating strong polar interactions.
	DFT (ESP Analysis)	Strong directional complementarity between positive ESP hydrogen atoms of RHB600′s –OH/–COOH and negative ESP oxygen atoms of DIN's NO_2 and C=O groups.
Lewis Acid-Base Interaction	XPS & FTIR	Shifts in binding energy and band intensity related to oxygen and nitrogen-containing groups suggest electron transfer.
	2D-COS	The early response of Si–O–Si and Si–OH groups suggest the involvement of mineral components in coordination.

4. Conclusions

This study systematically investigated the adsorption characteristics and mechanisms of dinotefuran (DIN) onto rice husk biochar (RHB) prepared at different pyrolysis temperatures (400–600 °C). The results demonstrate that pyrolysis temperature significantly modulates the physicochemical properties of biochar. RHB600, with its developed microporous structure, high aromaticity, and suitable oxygen-containing functional groups, exhibited the optimal DIN adsorption capacity (49.73 mg/g). The adsorption process followed the pseudo-second-order kinetic and Sips isotherm models, indicating a multilayer, heterogeneous adsorption process dominated by chemical interactions. The primary adsorption mechanisms involved the synergistic effects of pore-filling, π–π interactions, and hydrogen bonding. Among environmental factors, solution pH and humic acid concentration significantly influenced adsorption, while phosphate ions strongly inhibited removal via competitive adsorption. The artificial neural network (ANN) model outperformed response surface methodology (RSM) in predicting the interactive effects of multiple factors. Furthermore, RHB600 demonstrated good regenerability using ethanol as a desorbent, retaining 55% of its initial adsorption capacity after five consecutive adsorption–desorption cycles.

Beyond its effective adsorption performance, RHB600 presents a compelling practical advantage from a cost–benefit perspective. As evidenced in Table S4, the adsorption capacity of RHB600 (34.50 mg/g by Langmuir model; 49.73 mg/g by Sips model) is comparable to, and in many cases superior to, other reported adsorbents such as engineered biochar composites (e.g., 2.18 mg/g), magnetic nanosponges (0.92 mg/g), and aged microplastics (approx. 8–9 mg/g). More importantly, the primary feedstock—rice husks—is an abundant, low-cost, and globally available agricultural waste, the utilization of which also addresses solid waste management issues. This stands in stark contrast to adsorbents that rely on synthetic polymers, expensive chemicals, or complex manufacturing processes. Coupled with its good regenerability using a common solvent like ethanol, RHB600 emerges not only as a technically effective but also as an economically and environmentally sustainable option for decentralized or large-scale water treatment applications. In conclusion, rice husk biochar is an efficient and renewable adsorbent with potential application for remediating pesticide-contaminated water bodies.

5. Environmental Implications and Limitations

While this study demonstrates the high efficacy of RHB for DIN removal in controlled laboratory settings, its translation to real-world applications necessitates a discussion of environmental implications and inherent limitations.

Firstly, the end-of-life management of spent, pesticide-laden biochar is a critical consideration. After saturation, RHB600 constitutes a concentrated waste product requiring safe disposal or treatment. Landfilling poses a potential risk of pesticide leaching over time. Alternatively, regeneration (as shown in Section 3.7) offers a waste-minimization strategy, but the resulting concentrated desorbate still requires degradation, potentially via advanced oxidation processes. A promising, yet to be explored, route is the deliberate aging of the spent biochar in soil, where the strong adsorption capacity may gradually immobilize the pesticide, reducing its bioavailability while utilizing the carbon-rich material as a soil amendment.

Secondly, the potential leaching of soluble ash components from RHB, particularly under acidic conditions, warrants attention. Rice husk biochar contains inherent metal oxides (e.g., K, Ca, Mg). While our analysis confirmed the presence of these elements, their long-term stability in different environmental matrices (e.g., acid rain-affected soils or low-pH industrial wastewater) should be investigated in future studies to preclude any secondary contamination.

Finally, the performance in complex, real-world wastewater remains a key limitation of this work. Our experiments were conducted in idealized systems. Real agricultural runoff or industrial wastewater contains diverse dissolved organic matter, suspended solids, and a cocktail of other pesticides and pollutants, which could compete for adsorption sites or foul the biochar surface, potentially reducing efficiency. Therefore, future research must validate the performance of RHB in such complex matrices and develop pre-treatment steps or biochar modifications to enhance its selectivity and robustness in practical scenarios.

Supplementary Materials: The following supporting information can be downloaded at: https://www.mdpi.com/article/10.3390/agronomy15122746/s1, Figure S1. Artificial neural network architecture; Figure S2. Micromorphology of (a) RHB400, (b) RHB500, and (c) RHB600; Figure S3. The FTIR spectra of RHB; Figure S4. (a) Adsorption isotherm of DIN on RHB normalized by surface area, and (b) site adsorption energy (E^*) against DIN adsorption capacity of RHB; Figure S5. Adsorption isothermal data of DIN on RHB600 at different temperature, and the data was fitted by Sips model; Figure S6. Effects of (a) ionic strength, (b) co-existing anions, and (c) co-existing cations on DIN^+ adsorption by RHB600; Figure S7. (a) The speciation distributions of DIN versus pH in the aqueous solution and (b) the zeta potential of RHB600; Figure S8. Effect of solution pH and IS on adsorption capacity of RHB600: (a) were the response surface diagram of RHB600; (b) were the contour map of RHB600; Figure S9. Best validation performance plot of combined trained model; Figure S10. Effects of different desorbents on the cyclic adsorption–desorption of DIN by RHB600; Figure S11. Differential FTIR absorbance spectra of RHB600 with different DIN concentrations

(0–40 mg/L); Table S1. Different variable factors and their central combination designs at different levels; Table S2. The parameters of DIN adsorption on adsorbents simulated by adsorption kinetic models; Table S3. The parameters of DIN adsorption on adsorbents simulated by Langmuir, Freundlich and Sips models; Table S4. The maximum adsorption capacity of DIN on different adsorbents in previous studies; Table S5. Thermodynamics parameters for DIN adsorption on RHB600; Table S6. The parameters of DIN adsorption on RHB600 simulated by Sips models; Table S7. The initial and equilibrium solution pH values of electrolyte solution; Table S8. Experimental design matrix with observed and predicted values using RSM and ANN models; Table S9. ANOVA for response surface quadratic model. The Supplementary Materials include references [27,52,69–71].

Author Contributions: Conceptualization, L.L. and X.J.; methodology, L.L.; software, L.L. and T.L.; validation, X.J., T.L. and J.M.; data curation, L.L.; writing—original draft preparation, L.L.; writing—review and editing, L.L. and J.M.; visualization, J.M.; supervision, J.M.; project administration, L.L.; funding acquisition, L.L. All authors have read and agreed to the published version of the manuscript.

Funding: This research was funded by the National Natural Science Foundation of China, grant number 42407290.

Data Availability Statement: The original contributions presented in this study are included in the article/Supplementary Materials. Further inquiries can be directed to the corresponding author.

Conflicts of Interest: The authors declare no conflicts of interest.

Abbreviations

The following abbreviations are used in this manuscript:

RHB	Rice husk biochar
RHB400	Rice husk biochar pyrolyzed at 400 °C
RHB500	Rice husk biochar pyrolyzed at 500 °C
RHB600	Rice husk biochar pyrolyzed at 600 °C
NEOs	Neonicotinoid insecticides
DIN	Dinotefuran
SSA	Specific surface area
PV	Pore volume
2D-COS	Two-dimensional correlation spectroscopy
SED	Site energy distribution

References

1. Zhang, X.; Huang, Y.; Chen, W.-J.; Wu, S.; Lei, Q.; Zhou, Z.; Zhang, W.; Mishra, S.; Bhatt, P.; Chen, S. Environmental occurrence, toxicity concerns, and biodegradation of neonicotinoid insecticides. *Environ. Res.* **2023**, *218*, 114953. [CrossRef]
2. Alsafran, M.; Rizwan, M.; Usman, K.; Saleem, M.H.; Jabri, H.A. Neonicotinoid insecticides in the environment: A critical review of their distribution, transport, fate, and toxic effects. *J. Environ. Chem. Eng.* **2022**, *10*, 108485. [CrossRef]
3. Zhang, H.; Zhang, M.; Zhang, H.; Shen, X.; Lv, W.; Wang, X.; Zhang, J.; Guo, X. Bioaccumulation, transformation and toxicity of imidacloprid and dinotefuran in Eisenia fetida under single and binary exposure scenarios. *Environ. Toxicol. Pharmacol.* **2024**, *111*, 104570. [CrossRef] [PubMed]
4. Zhang, X.; Cao, Y.; Cao, J.; Li, Q.; Yan, Y. Occurrence; source, and risk assessment of neonicotinoid insecticides in the Huai River, China. *Environ. Pollut.* **2023**, *333*, 122068. [CrossRef] [PubMed]
5. Zhang, X.; Cao, Y.; Zhang, Z.; Li, Q.; Yan, Y. Residues of neonicotinoid insecticides in artificial waterways of the Eastern Route of the South-to North water diversion project, China: Implications for environmental risks and human health. *Environ. Pollut.* **2024**, *363*, 125132. [CrossRef] [PubMed]
6. Yang, Y.; Zhang, Q.; Xiao, Y.; Xiao, Y.; Gao, H.; Zhang, S.; Covaci, A.; Xia, X. Urban sewage discharge of neonicotinoids and their transformation products threatens aquatic organisms. *Water Res.* **2025**, *268*, 122740. [CrossRef]
7. Morrissey, C.A.; Mineau, P.; Devries, J.H.; Sanchez-Bayo, F.; Liess, M.; Cavallaro, M.C.; Liber, K. Neonicotinoid contamination of global surface waters and associated risk to aquatic invertebrates: A review. *Environ. Int.* **2015**, *74*, 291–303. [CrossRef]
8. Yokoyama, S.; Ito, M.; Nagasawa, S.; Morohashi, M.; Ohno, M.; Todate, Y.; Kose, T.; Kawata, K. Runoff and Degradation of Aerially Applied Dinotefuran in Paddy Fields and River. *Bull. Environ. Contam. Toxicol.* **2015**, *94*, 796–800. [CrossRef]

9. Tang, T.; Cui, W.; Wei, D.; Yu, S.; Lu, Z.; Quan, Z. An integrated assessment and spatial-temporal variation analysis of neonicotinoids in pollen and honey from noncrop plants in Zhejiang, China. *Environ. Pollut.* **2019**, *250*, 397–406. [CrossRef]
10. Lung, I.; Soran, M.-L.; Stegarescu, A.; Opriş, O. Devrinol and triadimefon removal from aqueous solutions using CNT-COOH/MnO_2/Fe_3O_4 nanocomposite. *J. Iran. Chem. Soc.* **2022**, *19*, 2031–2039. [CrossRef]
11. Ni, Z.; Chen, Z.; Zhang, X.; Yang, X.; Zhou, L. Photolysis of fungicide triadimefon: A combined experimental and theoretical investigation on homolytic CO and CN bonds dissociation mechanisms. *J. Photochem. Photobiol. A Chem.* **2023**, *436*, 114402. [CrossRef]
12. Diao, Z.-H.; Yan, L.; Dong, F.-X.; Qian, W.; Deng, Q.-H.; Kong, L.-J.; Yang, J.-W.; Lei, Z.-X.; Du, J.-J.; Chu, W. Degradation of 2,4-dichlorophenol by a novel iron based system and its synergism with Cd(II) immobilization in a contaminated soil. *Chem. Eng. J.* **2020**, *379*, 122313. [CrossRef]
13. Cui, S.; Lv, J.; Hough, R.; Fu, Q.; An, L.; Zhang, Z.; Ke, Y.; Liu, Z.; Li, Y.-F. Recent advances and prospects of neonicotinoid insecticides removal from aquatic environments using biochar: Adsorption and degradation mechanisms. *Sci. Total Environ.* **2024**, *939*, 173509. [CrossRef]
14. Feng, D.; Dai, J.; Zhu, Z.; Huo, P.; Yan, Y.; Li, C. Molecularly imprinted electrochemical sensor arrays combined with machine learning for simultaneous determination of three neonicotinoid insecticides. *Chin. Chem. Lett.* **2025**, 111789. [CrossRef]
15. Ajermoun, N.; Haddioui, L.; Bard, A.; Laghrib, F.; Farahi, A.; Lahrich, S.; Bakasse, M.; Saqrane, S.; Abderrahim El Mhammedi, M. Environmental and human health impacts of neonicotinoid insecticides: A review. *Pedosphere* **2025**. [CrossRef]
16. Zhao, H.; Xiang, X.; Zhang, H.; Chen, J.; Yang, M.; Chen, H.; Tian, X. Straw and its biochar differently affect soil bacteria community composition, co-occurrence network and function in Cd-contaminated soil. *J. Environ. Chem. Eng.* **2025**, *13*, 116409. [CrossRef]
17. Šunta, U.; Prosenc, F.; Trebše, P.; Bulc, T.G.; Kralj, M.B. Adsorption of acetamiprid, chlorantraniliprole and flubendiamide on different type of microplastics present in alluvial soil. *Chemosphere* **2020**, *261*, 127762. [CrossRef]
18. Cao, Y.; Jiang, S.; Zhang, Y.; Xu, J.; Qiu, L.; Wang, L. Investigation into adsorption characteristics and mechanism of atrazine on nano-MgO modified fallen leaf biochar. *J. Environ. Chem. Eng.* **2021**, *9*, 105727. [CrossRef]
19. Flores, F.M.; Undabeytia, T.; Jaworski, M.; Morillo, E.; Sánchez, R. Organo-montmorillonites as adsorbent materials for thiophanate-methyl removal: Adsorption-desorption studies and technological applications. *J. Environ. Chem. Eng.* **2020**, *8*, 103806. [CrossRef]
20. Choudhury, P.; Manna, M.S.; Nag, S. A critical review on green synthesis and modification techniques of biochar: Comparison of efficacies towards adsorption capacities. *Biomass Bioenergy* **2025**, *198*, 107859. [CrossRef]
21. Cui, Q.; Xia, J.; Yang, H.; Liu, J.; Shao, P. Biochar and effective microorganisms promote Sesbania cannabina growth and soil quality in the coastal saline-alkali soil of the Yellow River Delta, China. *Sci. Total Environ.* **2021**, *756*, 143801. [CrossRef] [PubMed]
22. Foong, S.Y.; Chan, Y.H.; Chin, B.L.F.; Lock, S.S.M.; Yee, C.Y.; Yiin, C.L.; Peng, W.; Lam, S.S. Production of biochar from rice straw and its application for wastewater remediation—An overview. *Bioresour. Technol.* **2022**, *360*, 127588. [CrossRef] [PubMed]
23. Apolloni, F.; Menegazzo, F.; Bittencourt, C.; Signoretto, M. Hazelnut shells and rice husks activated biochars for the adsorption of atrazine and terbuthylazine. *Next Energy* **2025**, *7*, 100291. [CrossRef]
24. Rezvani, B.; Hallajisani, A.; Tavakoli, O. Super-effective biochar adsorbents from Co-pyrolysis of rice husk and sewage sludge: Adsorption performance, advanced regeneration, and economic analysis. *Bioresour. Technol. Rep.* **2025**, *29*, 102046. [CrossRef]
25. Zhang, Z.; Zhang, S.; Ren, D.; Zhang, X.; Tang, K.; Zhang, X. Adsorption characteristic of Cd2+ on the nano-hydroxyapatite/biochar hybrid materials derived from rice husk and eggshells. *Desalin. Water Treat.* **2023**, *287*, 182–190. [CrossRef]
26. Shi, Y.; Wang, S.; Xu, M.; Yan, X.; Huang, J.; Wang, H.-W. Removal of neonicotinoid pesticides by adsorption on modified Tenebrio molitor frass biochar: Kinetics and mechanism. *Sep. Purif. Technol.* **2022**, *297*, 121506. [CrossRef]
27. Chen, X.; Yao, X.-W.; Diao, Y.; Liu, H.; Chen, M.-L.; Feng, N.-J.; Qian, W.; Zhou, X.-H.; Guo, P.-R.; Kong, L.-J.; et al. Simultaneous removal of triadimefon and dinotefuran by a new biochar-based magnesium oxide composite in water: Performances and mechanism. *Sep. Purif. Technol.* **2024**, *336*, 126213. [CrossRef]
28. He, J.; Guo, J.; Zhou, Q.; Fang, F. Adsorption characteristics of nitrite on natural filter medium: Kinetic, equilibrium, and site energy distribution studies. *Ecotoxicol. Environ. Saf.* **2019**, *169*, 435–441. [CrossRef]
29. Liu, L.; Che, N.; Wang, S.; Liu, Y.; Li, C. Copper Nanoparticle Loading and F Doping of Graphene Aerogel Enhance Its Adsorption of Aqueous Perfluorooctanoic Acid. *ACS Omega* **2021**, *6*, 7073–7085. [CrossRef]
30. Ramanathan, T.; Sathasivan, A. Dissolved organic carbon concentration changes in surface drinking water sources, treatment challenges and potential solutions—A review. *J. Water Process Eng.* **2025**, *76*, 108188. [CrossRef]
31. Yan, Y.; Wan, B.; Mansor, M.; Wang, X.; Zhang, Q.; Kappler, A.; Feng, X. Co-sorption of metal ions and inorganic anions/organic ligands on environmental minerals: A review. *Sci. Total Environ.* **2022**, *803*, 149918. [CrossRef]

32. Zhang, Z.; Li, Y.; Zong, Y.; Yu, J.; Ding, H.; Kong, Y.; Ma, J.; Ding, L. Efficient removal of cadmium by salts modified-biochar: Performance assessment, theoretical calculation, and quantitative mechanism analysis. *Bioresour. Technol.* **2022**, *361*, 127717. [CrossRef] [PubMed]
33. Grimme, S.; Antony, J.; Ehrlich, S.; Krieg, H. A consistent and accurate ab initio parametrization of density functional dispersion correction (DFT-D) for the 94 elements H-Pu. *J. Chem. Phys.* **2010**, *132*, 154104. [CrossRef] [PubMed]
34. Cantou, G.; Wang, J.J.; Zhou, B.; Lee, J.-M.; Park, J.-H. Toxicological fate of biochar according to feedstock and pyrolysis temperature. *Ind. Crops Prod.* **2025**, *236*, 122094. [CrossRef]
35. Subbiah, G.; Singh, R.P.; Deepak, K.; Nayak, P.P.; venkadeshwaran, K.; Tiwari, A.; Sahoo, J.; Priya, K. Continuous pyrolysis of rice husk for sustainable biochar production and carbon sequestration: Recent advances and techno-economic perspectives. *Results Eng.* **2025**, *27*, 106991. [CrossRef]
36. Aziz, K.H.H.; Mustafa, F.S.; Karim, M.A.H.; Hama, S. Biochar-based catalysts: An efficient and sustainable approach for water remediation from organic pollutants via advanced oxidation processes. *J. Environ. Manag.* **2025**, *390*, 126245. [CrossRef]
37. Rahman, M.M.; Maniruzzaman, M.; ealam, N.; Mahmud, P.; Khatun, S.; Hossain, M.K.; Hossain, M.I.; Hasanuzzaman, M.; Alam, M.A.; Al-amin, M.; et al. Adsorptive removal of toxic heavy metal and dyes from wastewater by rice husk (lignocellulosic biomass) derived activated biochar: A fixed-bed column adsorption study. *Carbohydr. Polym. Technol. Appl.* **2025**, *9*, 100698. [CrossRef]
38. Chen, S.; Wang, T.; Chen, C.; Liu, J.; Mei, M.; Xie, J.; Li, J. Study on adsorption of Direct Red 23 by biochar derived from co-pyrolysis of sewage sludge and rice husk waste: Optimization, isotherm, kinetic, thermodynamic and mechanisms. *Desalin. Water Treat.* **2021**, *221*, 378–395. [CrossRef]
39. Chen, B.; Li, C.; Song, J.; Dai, X.; Lu, Z.; Zhou, Z.; Wang, Q.; Dai, L. Removal of Cl- from contaminated acid by resin adsorption: Kinetics, isothermal model, approximate site energy distribution and adsorption mechanism. *J. Environ. Chem. Eng.* **2025**, *13*, 116656. [CrossRef]
40. Petrović, J.; Koprivica, M.; Ercegović, M.; Simić, M.; Dimitrijević, J.; Bugarčić, M.; Trifunović, S. Synthesis and Application of FeMg-Modified Hydrochar for Efficient Removal of Lead Ions from Aqueous Solution. *Processes* **2025**, *13*, 2060. [CrossRef]
41. Reguyal, F.; Sarmah, A.K. Site energy distribution analysis and influence of Fe_3O_4 nanoparticles on sulfamethoxazole sorption in aqueous solution by magnetic pine sawdust biochar. *Environ. Pollut.* **2018**, *233*, 510–519. [CrossRef]
42. Chen, Y.; Li, L.; Yang, Y.; Wang, C.; Zhang, Q. Immobilization of laccase on biochar for the remediation of organic pollutants: A comprehensive review. *Int. J. Biol. Macromol.* **2025**, *322*, 146778. [CrossRef] [PubMed]
43. Chen, P.; Shi, M.; Liu, X.; Wang, X.; Fang, M.; Guo, Z.; Wu, X.; Wang, Y. Comparison of the binding interactions of 4-hydroxyphenylpyruvate dioxygenase inhibitor herbicides with humic acid: Insights from multispectroscopic techniques, DFT and 2D-COS-FTIR. *Ecotoxicol. Environ. Saf.* **2022**, *239*, 113699. [CrossRef] [PubMed]
44. Islam, M.T.; Hossen, M.F.; Kudrat-E-Zahan, M.; Asraf, M.A.; Zakaria, C.M.; Hayatullah; Rana, M.S. Effect of temperature and time on purity, morphology and phase transformations of silica from rice husk. *Chem. Inorg. Mater.* **2025**, *5*, 100092. [CrossRef]
45. Wu, Y.; Gui, Q.; Zhang, H.; Li, H.; Li, B.; Liu, M.; Chen, Y.; Zhang, S.; Yang, H.; Chen, H. Effect of biomass components' interaction on the pyrolysis reaction kinetics and small-molecule product release characteristics. *J. Anal. Appl. Pyrolysis* **2023**, *173*, 106039. [CrossRef]
46. Sun, J.; Yan, W.; Liu, X.; Hu, T.; Xiong, Y.; Tian, S.; Feng, J.; Huang, Z.; Zhao, Z. Rice husk waste-derived super-biochar with the max surface area and Philic-CO2 textural structure: Boosting effect and mechanism of post-desilication. *Chem. Eng. J.* **2024**, *490*, 151583. [CrossRef]
47. Zhang, P.; Wang, B.; Liu, H.; Rui, Y.; Li, G.; Zhang, J. Biomass pyrolysis characterisation based on machine learning: Identification of key factors affecting biochar stability. *Biomass Bioenergy* **2025**, *203*, 108293. [CrossRef]
48. Tan, H.; Chiew, C.H.; Guo, S.-R.; Li, L.; Lim, L.Y.; Ong, P.Y.; Wong, K.Y.; Li, C.; Varbanov, P.S.; Lee, C.T. Prediction of biochar physicochemical properties based on biomass initial conditions and pyrolysis process supported by data-driven multiple linear regression model. *Energy* **2025**, *340*, 139304. [CrossRef]
49. Yu, B.; Liu, D.; Bian, Z.; Yang, F.; Gao, H.; Arvola, L. Identifying degradation mechanism of dissolved and particular organic matter by novelty hetero-2D-COS during petrochemical wastewater treatment. *J. Water Process Eng.* **2025**, *71*, 107299. [CrossRef]
50. Ma, Y.; Chen, S.; Qi, Y.; Yang, L.; Wu, L.; He, L.; Li, P.; Qi, X.; Gao, F.; Ding, Y.; et al. An efficient, green and sustainable potassium hydroxide activated magnetic corn cob biochar for imidacloprid removal. *Chemosphere* **2022**, *291*, 132707. [CrossRef]
51. Liu, L.; Liu, Y.; Che, N.; Gao, B.; Li, C. Electrochemical adsorption of perfluorooctanoic acid on a novel reduced graphene oxide aerogel loaded with Cu nanoparticles and fluorine. *J. Hazard. Mater.* **2021**, *416*, 125866. [CrossRef]
52. Yang, J.; Chen, A.; Zhu, S.; Shang, C.; Yang, Z.; Cao, L.; Bai, M. Adsorption behavior of neonicotinoid pesticides on typical soil minerals. *J. Environ. Chem. Eng.* **2025**, *13*, 116939. [CrossRef]
53. Tan, Q.; Chen, Z.; Shen, J.; Yan, P.; Kang, J.; Wang, B.; Zhao, S.; Shen, Y.; Li, Y. In situ construction of ZnFe-layered double oxides on biochar for improving interfacial adsorption-catalysis of ozone achieves efficient water purification. *Sep. Purif. Technol.* **2026**, *380*, 135358. [CrossRef]

54. Zhang, D.; Zhang, K.; Hu, X.; He, Q.; Yan, J.; Xue, Y. Cadmium removal by MgCl2 modified biochar derived from crayfish shell waste: Batch adsorption, response surface analysis and fixed bed filtration. *J. Hazard. Mater.* **2021**, *408*, 124860. [CrossRef] [PubMed]
55. Yamaguchi, A.; Ishii, A.; Kamijo, T. Influence of ionic strength and temperature on adsorption of tetrakis-N-methylpyridyl porphyrin onto mesoporous silica. *Colloids Surf. A Physicochem. Eng. Asp.* **2022**, *655*, 130262. [CrossRef]
56. Jiang, H.; Ma, J.; Zhang, M.; Dai, Y.; Wang, Y.; Huang, H.; Yuan, S.; Li, K.; Zhou, T.; Lv, R.; et al. Calcium carbonate self fixed crayfish shell composite biochar for removing tetracycline from water. *Colloids Surf. A Physicochem. Eng. Asp.* **2025**, *711*, 136371. [CrossRef]
57. Wang, B.; Hu, X.; Li, L.; Wang, H.; Huang, H.; Wang, R.; Zhou, D.; Yuan, J.; Chen, L. Application and functionalization of toxic waste sludge-derived biochar for efficient phosphate separation from aqueous media: Toxicity diminution, robust adsorption, and inner mechanism. *Chem. Eng. J.* **2023**, *468*, 143745. [CrossRef]
58. Chen, H.; Gao, Y.; Li, J.; Sun, C.; Sarkar, B.; Bhatnagar, A.; Bolan, N.; Yang, X.; Meng, J.; Liu, Z.; et al. Insights into simultaneous adsorption and oxidation of antimonite [Sb(III)] by crawfish shell-derived biochar: Spectroscopic investigation and theoretical calculations. *Biochar* **2022**, *4*, 37. [CrossRef]
59. Priya, E.; Kumar, S.; Verma, C.; Sarkar, S.; Maji, P.K. A comprehensive review on technological advances of adsorption for removing nitrate and phosphate from waste water. *J. Water Process Eng.* **2022**, *49*, 103159. [CrossRef]
60. Yazdi, F.; Anbia, M.; Sepehrian, M. Recent advances in removal of inorganic anions from water by chitosan-based composites: A comprehensive review. *Carbohydr. Polym.* **2023**, *320*, 121230. [CrossRef]
61. Li, S.; Yang, M.; Wang, H.; Jiang, Y. Adsorption of microplastics on aquifer media: Effects of the action time, initial concentration, ionic strength, ionic types and dissolved organic matter. *Environ. Pollut.* **2022**, *308*, 119482. [CrossRef]
62. Liu, L.; Yan, H.; Tan, W.; Zhu, G. Influence of Na^+, K^+, Mg^{2+}, Ca^{2+}, and Fe^{3+} on filterability and settleability of drilling sludge. *Chin. J. Chem. Eng.* **2017**, *25*, 658–664. [CrossRef]
63. Geysels, B.; Hiemstra, T.; Vermeer, A.W.P.; Groenenberg, J.E. A mechanistic surface complexation model for glyphosate adsorption to ferrihydrite in competition with phosphate. *Water Res.* **2026**, *288*, 124634. [CrossRef] [PubMed]
64. Feng, Y.; Jabbarzadeh, A. Enhancing metal surface adsorption and tribological performance of water-based ionic liquid lubricants: The role of amino acid types. *Appl. Surf. Sci.* **2025**, *713*, 163711. [CrossRef]
65. Foroutan, R.; Peighambardoust, S.J.; Mohammadi, R.; Omidvar, M.; Sorial, G.A.; Ramavandi, B. Influence of chitosan and magnetic iron nanoparticles on chromium adsorption behavior of natural clay: Adaptive neuro-fuzzy inference modeling. *Int. J. Biol. Macromol.* **2020**, *151*, 355–365. [CrossRef]
66. Simić, V.M.; Rajković, K.M.; Stojičević, S.S.; Veličković, D.T.; Nikolić, N.Č.; Lazić, M.L.; Karabegović, I.T. Optimization of microwave-assisted extraction of total polyphenolic compounds from chokeberries by response surface methodology and artificial neural network. *Sep. Purif. Technol.* **2016**, *160*, 89–97. [CrossRef]
67. Kalisz, O.; Hulicka, G.; Tobiszewski, M.; Bocian, S. Performance evaluation of green and conventional solvents in reversed-phase liquid chromatography based on the separation of non-polar and polar substances. *Green Chem.* **2024**, *27*, 3020–3031. [CrossRef]
68. Pan, D.; Wu, X.; Chen, P.; Zhao, Z.; Fan, F.; Wang, Y.; Zhu, M.; Xue, J.; Wang, Y. New insights into the interactions between humic acid and three neonicotinoid pesticides, with multiple spectroscopy technologies, two-dimensional correlation spectroscopy analysis and density functional theory. *Sci. Total Environ.* **2021**, *798*, 149237. [CrossRef]
69. El-Aswad, A.F.; Aly, M.I.; Fouad, M.R.; Badawy, M.E.I. Adsorption and thermodynamic parameters of chlorantraniliprole and dinotefuran on clay loam soil with difference in particle size and pH. *J. Environ. Sci. Health Part B* **2019**, *54*, 475–488. [CrossRef]
70. Salazar, S.; Yutronic, N.; Jara, P. Magnetic β-Cyclodextrin Nanosponges for Potential Application in the Removal of the Neonicotinoid Dinotefuran from Wastewater. *Int. J. Mol. Sci.* **2020**, *21*, 4079. [CrossRef]
71. Zhang, Q.; Xu, P.; Yan, N.; Ren, Y.; Liang, X.; Guo, X. Adsorption of neonicotinoid insecticides by mulch film-derived microplastics and their combined toxicity. *Sci. Total Environ.* **2024**, *955*, 177238. [CrossRef] [PubMed]